SURFACE AND INTERFACE ANALYSIS

1. Overview of Surface and Interface Analysis Methods

Surfaces and interfaces play an increasing role in advanced materials science and technology. Owing to the considerable refinement of measurement techniques in the past three decades, the characteristics of surfaces and interfaces can be analyzed using an abundant variety of methods. As significant advances in instrumentation are realized, new and improved methods for surface and interface analysis will emerge. Given the scope of modern surface and interfacial analysis, all of the methods used for study cannot be comprehensively treated here. Therefore, the focus of this article will be on those methods that are estimated by the author to be of the greatest importance. The interested reader is referred to numerous other compendiums of information on this broad topic (1–4). Particularly noteworthy are the series of Fundamental Reviews on specific techniques that appear biennially in the journal *Analytical Chemistry*. These Reviews report developments in specific fields since the previous report, and usually they provide an up-to-date perspective of significant advances made in the field. Of particular relevance to this article are the Fundamental Reviews on surface analysis, scanning probe microscopy, and IR spectroscopy that have appeared recently (5).

According to the ISO vocabulary (18115: 2001, Surface chemical analysis—Vocabulary, International Organization for Standardization, Geneva, 2001), an interface is defined as a boundary between two bulk phases having different chemical, elemental, or physical properties (more precisely, this is a hetero-interface, whereas a homo-interface is an interface between two identical phases distinguished, for example, only by different crystalline orientations, as for grain boundaries in pure metals). A surface is defined, after ISO, as an interface between a condensed phase and a gas, vapor, or free space. For example, the surface of an ice cube on air transforms, when put in a glass of water, in an interface between two condensed phases that are identical in chemical composition. The surface of a straw in the same glass of water represents an example of an interface between chemically distinct materials.

The chemical, structural, and electronic characteristics of surfaces and interfaces are usually different from those of the bulk phase(s). Thus, methods to be used for the analysis of surfaces must be selective in response to the surface or interfacial region relative to the bulk. Surfaces and interfaces are most commonly explored using techniques based on the interaction of photons, electrons, or ions with the surface or using a force such as an electric field or van der Waals attraction. These excitations generate a response involving the production of photons, electrons, ions, or the alteration of a force that is then sensed in the analysis.

The choice of which of these exciting species or forces, and hence technique, to use depends on the nature of the information sought about the surface. This article is organized around a discussion of techniques that can be used to answer

the following important fundamental questions that are typically asked about surfaces and interfaces:

What is the morphology and structure of the surface or interface?
What is the elemental composition of the surface or interface?
What are the chemical bonds and/or the electronic and molecular structure of the surface or the interface?

Table 1 provides an overview of many of the techniques available for the characterization of surfaces and interfaces. These techniques are categorized on the basis of the nature of the exciting and detected species (or force). As can be seen by Table 1, a tremendous number of approaches are available for the study of surfaces. In fact, multiple methods capable of answering all of the three questions posed above have been developed over the past 30 years.

Several methods using photons as the exciting and detected species are commonly employed. Ellipsometry provides information about thin-film thickness, typically using visible wavelength light. Information about the vibrational modes of molecules at surfaces or within interfaces can be obtained using one of several vibrational spectroscopies, including transmission Fourier transform infrared spectroscopy (FTIR), diffuse reflectance infrared Fourier transform spectroscopy (DRIFT), Infrared reflection–absorption spectroscopy (IRRAS), Raman spectroscopy, surface-enhanced Raman scattering (SERS), or sum-frequency generation (SFG). These approaches are based on visible or infrared wavelength photons that are either absorbed, scattered, or generated. X-ray diffraction (XRD) is a common technique for the determination of the atomic structure. When applied under grazing incidence angle and therefore approaching total reflection (typically 0.2° from the surface plane) in the technique of grazing incidence x-ray diffraction (GIXRD), it is a surface structural technique that relies on the diffraction of x-ray wavelength photons. Analogously, total reflection x-ray fluorescence (TXRF) provides a means to analyze the top 5 nm of a smooth sample with high sensitivity. Extended x-ray absorption fine structure (EXAFS) is a technique in which the x-ray absorption cross section of a material is modulated by the local surface structure and/or coordination environment of an atom. This modulation is detected by either x-ray fluorescence or attenuation of the incident x-ray beam. The x-ray absorption near edge structure (XANES) provides additional information to determine the geometrical arrangement of the atoms surrounding the absorbing atom. In versions of EXAFS that are more surface sensitive, near-edge x-ray absorption fine structure (NEXAFS) or surface extended x-ray absorption fine structure (SEXAFS), x-ray absorption is modulated by surface structure as sensed by monitoring photoemitted or Auger electrons.

Other techniques in which incident photons excite the surface to produce detected electrons are also listed in Table 1. X-ray photoelectron spectroscopy (XPS), which is also known as electron spectroscopy for chemical analysis (ESCA), is based on the use of x rays that cause atomic core level electron ejection for elemental composition information. Ultraviolet photoelectron spectroscopy (UPS) is similar but uses ultraviolet photons instead of x rays to probe atomic valence level electrons. Photons are used to stimulate desorption of ions in

Table 1. **Overview of Common Surface Analysis Techniques**[a]

	Detection			
Excitation	Photons	Electrons	Ions	Force
photons	ellipsometry FTIR, IRRAS, DRIFT Raman, SERS SHG, SFG XRD EXAFS, NEXAFS, SEXAFS	XPS (ESCA) UPS	PSD	
electrons	IP	SEM, FE-SEM, TEM, STEM AES, APS LEED, RHEED EELS, HREELS, CEELS	ESDIAD	
ions		INS	SIMS ISS, RBS LEIS	
force		FEM STM	FIM	AFM

[a]Key to abbreviations.
FTIR = Fourier transform infrared spectroscopy.
IRRAS = infrared reflection absorption spectroscopy.
DRIFT = diffuse reflectance infrared Fourier transform spectroscopy.
SERS = surface-enhanced Raman scattering.
SHG = second harmonic generation.
SFG = sum-frequency generation.
XRD = x-ray diffraction.
EXAFS = extended x-ray absorption fine structure.
NEXAFS = near-edge x-ray absorption fine structure.
SEXAFS = surface extended x-ray absorption fine structure.
XPS = x-ray photoelectron spectroscopy.
ESCA = electron spectroscopy for chemical analysis.
UPS = ultraviolet photoelectron spectroscopy.
PSD = photon stimulated ion angular distribution.
IP = inverse photoemission.
SEM = scanning (or secondary) electron microscopy.
FE-SEM = field emission scanning electron microscopy.
TEM = transmission electron microscopy.
STEM = scanning transmission electron microscopy.
AES = Auger electron spectroscopy.
APS = appearance potential spectroscopy.
LEED = low-energy electron diffraction.
RHEED = reflected high-energy electron diffraction.
EELS = electron energy loss spectroscopy.
HREELS = high-resolution electron energy loss spectroscopy.
CEELS = core-level electron energy loss spectroscopy.
ESDIAD = electron-stimulated ion angular distribution.
INS = ion neutralization spectroscopy.
SIMS = secondary ion mass spectroscopy.
ISS = ion scattering spectroscopy.
RBS = Rutherford backscattering spectroscopy.
LEIS = low-energy ion scattering.
FEM = field emission microscopy.
FIM = field ion microscopy.
AFM = atomic force microscopy.
STM = scanning tunneling microscopy.

photon stimulated desorption (PSD). Inverse photoemission spectroscopy (IPES) occurs when electrons incident on a surface result in emission of photons that are then energetically analyzed. This energy corresponds to the difference between the electron energy and that of unoccupied electron levels above the Fermi edge.

Electrons are used for excitation and detection in the various electron microscopy methods for surface visualization and imaging [scanning electron microscopy (SEM), field emission scanning electron microscopy (FE-SEM), transmission electron microscopy (TEM), and scanning transmission electron microscopy (STEM)], the electron diffraction methods for the determination of surface atomic structure [low-energy electron diffraction (LEED), reflection high-energy electron diffraction (RHEED)], and the electron energy loss spectroscopies for evaluation of surface electronic and chemical characteristics [electron energy loss spectroscopy (EELS), high-resolution electron energy loss spectroscopy (HREELS), and core level electron energy loss spectroscopy (CEELS)]. Ions produced by electron-stimulated desorption are measured in electron-stimulated desorption-ion angular distribution (ESDIAD). If neutralization of an incident ion beam is measured by surface electron ejection, the technique of ion neutralization spectroscopy (INS) results.

Ions can also be used as both the excitation and the detection species in several surface analysis techniques. In secondary ion mass spectroscopy (SIMS), an incident beam of ions can sputter molecular ions from a surface providing surface elemental and molecular information. Ions can be scattered from surfaces or within interfaces in ion scattering spectroscopy (ISS) or low-energy ion scattering (LEIS) to provide elemental composition and structural information of the first surface layer, whereas medium-energy ion scattering (MEIS) and high-energy ion scattering (HEIS) or Rutherford backscattering spectroscopy (RBS) probe deeper layers up to several micrometers. Finally, an electric field can be used to stimulate ionization of an imaging gas in field ion microscopy (FIM) or electron tunneling in field emission microscopy (FEM) and scanning tunneling microscopy (STM) for surface imaging. A surface imaging technique that uses van der Waals forces as the "excitation" while monitoring what are essentially drag or frictional forces is atomic force microscopy (AFM).

In choosing appropriate techniques with which to interrogate surfaces in search of answers to the above three questions, one must remain cognizant of the lateral resolution and depth at which the chemistry of interest occurs as well as the lateral resolution and depth sensitivity of each technique. Photon beams cannot be focused as tightly as electron or ion beams, for example, implying that techniques using photon beams will have poorer lateral resolution than techniques using electron beams. This characteristic may or may not be a limitation, however, depending on the scale on which the surface chemistry of interest is occurring.

Depth sensitivity is an equally important consideration in the analysis of surfaces. Techniques based on the detection of electrons or ions derive their surface sensitivity from the fact that these species cannot travel long distances in solids without undergoing interactions that cause energy loss. If electrons are used as the basis of an analysis, the information depth will be relatively shallow and depends on both the energy of the incident and the detected electrons and on the characteristics of the material. In contrast, analysis techniques based on

high-energy photons such as x rays will, in general (with TXRF as an exception, see above), sample a much larger depth, as compared with electrons of the same energy, because x rays can travel longer distances in solids. Therefore, the depth sensitivity of a particular method will depend on the nature and energy of both the probe and the detected species, and they may or may not be sensitive to the entire depth to which the chemistry of interest occurs.

Although not a universal requirement of surface analysis, techniques that use electron or ion beams must be carried out in ultra-high-vacuum (UHV) environments wherein the pressures are kept lower than ca 10^{-8} Pa. These extremely low pressures ensure not only that electrons and ions can travel undisturbed to a surface, and the excited species to the analyzer, but also that the analyzed surface is kept free of distortional surface reactions and contaminations. Vacuum technology is significantly advanced such that these pressures can be routinely achieved and maintained as a matter of course with adequate pumping in usually rigorously clean, leak-free, stainless steel environments. A variety of pumps exist that can pump down to UHV pressures with turbomolecular, ion, diffusion, and cryo pumps being the most common. Each of these pumps possesses its own advantages and disadvantages. The interested reader is referred to Ref. 6 for a more comprehensive treatment of modern vacuum technology.

2. Techniques

2.1. Imaging of Surfaces—Analysis of Surface Morphology. Several important techniques can help answer the question: What does the surface look like? This question is often the first one to be posed in the characterization of a new surface or interface. Physical imaging of the surface is necessary to distinguish the relevant features important for understanding the whole surface and is essential for accurate interpretation of data from other surface analysis techniques that might later be applied to a more limited region of the surface or interface.

Electron Microscopy. The techniques of primary importance in surface and interface imaging are the electron microscopies (7–12). These techniques take advantage of the fact that accelerated beams of electrons typically have higher energies than commonly available photon beams, and therefore, they can be focused more tightly. For example, consider two electron beams of 10 keV and 40 keV energy, respectively. Using the fact that $E = hc/\lambda$, the wavelength λ of the electrons in each beam are calculated to be 0.124 and 0.03 nm, respectively, much shorter than even x-ray beams. For surface imaging applications, the consequence of this wavelength is realized in terms of the lateral resolution that can be attained. Assuming that these beams are perfectly focused, the theoretically best resolution that can be achieved is of the order of $\lambda/2$ or ca 0.06 nm for the 10-keV beam and 0.015 nm for the 40-keV beam. Although this resolution is never attainable in reality due to limitations of electron lenses, these calculations serve to demonstrate the importance of using high-energy beams for physical imaging on the atomic scale in electron microscopy.

Electron microscopy is done in one of two ways: SEM or TEM (8). STEM is simply TEM carried out in a scanning mode. SEM is the most common and

well-known electron microscopy method for the physical imaging of surfaces. This technique is based on the interaction with a surface of a primary beam of electrons with energy typically in the range of 0.5–40 keV. This primary electron beam is first demagnified by a condenser lens and then focused onto the sample surface using a series of objective lenses where it is rastered across the surface using a series of scanning coils. SEM must be done in vacuum so that the electrons can travel unimpeded for adequate distances. The typical surface magnification realized is of the order of 10–100,000 times depending on the energy of the primary electron beam in traditional SEM instruments. However, modern SEMs can achieve a lateral resolution of 1.5 nm at a primary electron voltage of only 1.5 keV.

In most SEM analyses, secondary electrons created near the position of the impinging primary beam are detected. However, surface images can also be obtained through collection of backscattered primary electrons. The secondary electrons, which result from ionization of the sample atoms in the near-surface region by the incident or backscattered primary electrons, have much smaller energies of ca 0–20 eV. Various mechanisms result in the ejection of these secondary electrons from the surface. However, due to their very low energies, secondary electrons have escape depths of only a few nanometers. Therefore, SEM is a highly surface-sensitive tool, even if the primary beam electrons may penetrate into the sample to depths of up to 5 μm for higher voltages.

The efficiency of secondary electron creation, therefore, becomes important in sensitivity. For a given nature and morphology of the sample, the yield of secondary electrons per primary electron is dictated primarily by the primary beam energy and incidence angle and by the angle of collection. The secondary electron yield actually shows a slight negative dependence on primary beam energy because the higher the primary beam energy, the deeper its penetration and the less efficient is the secondary electron escape from the surface. Thus, the secondary electron yield varies as ca $E^{-0.8}$ for primary beam energy E. In addition, the secondary electron yield depends on angle of collection, generally increasing as the angle from the surface normal increases.

Given the option to obtain images by collection of either secondary electrons or backscattered primary electrons, one might reasonably ask which is the better strategy for surface imaging. Both approaches have strengths and weaknesses depending on the information desired. Generally, images from secondary electrons have higher resolution, because they depend only on the primary beam diameter. Secondary electron images also have higher contrast than backscattered electron images. However, backscattered electron images have their own set of advantages. Chief among these is that backscattered electron images are generally more sensitive to topography than secondary electron images, because backscattering increases significantly at sharp edges on a surface. Backscattering efficiency is a function of the atomic number (Z) of the atom from which the backscattering occurs. Thus, backscattered images have a pronounced dependence on the elemental composition of the sample surface. Secondary electron images actually have a slight dependence on elemental composition as well, because some of the secondary electrons are generated by backscattered primary electrons. When acquiring backscattered electron images, either of these attributes can be maximally exploited by the manner in which the collected backscattered

electrons are processed. Backscattered electrons are detected with a two-half annular detector. Images sensitive to elemental composition differences across the surface are obtained when the electron intensities in each half of the detector are added. In contrast, images sensitive to surface topography are obtained by subtracting the electron intensities in each half of the detector.

Backscattered electrons are diffracted by the crystallographic planes, and the diffracted beam produces a pattern composed of intersecting bands (so-called Kikuchi lines). These electron backscatter patterns, or EBSPs, can be imaged by placing a suitable phosphor screen in close proximity to the sample in the SEM sample chamber. Analyzing the pattern and bands provides information about the crystal structure for the measured phase, including symmetry of the lattice, spacing of atoms, and local orientation of the crystal lattice with respect to the laboratory reference. Thus, in polycrystalline materials, an orientation distribution of the grains can be obtained with the technique of orientation image microscopy (OIM) (9).

A block diagram of a scanning electron microscope is shown in Figure 1. A vacuum on the order of ca 10^{-5} Pa is required to ensure adequate electron pathlengths. This level of vacuum is readily attainable with diffusion pumps trapped with liquid nitrogen.

The electron sources used in most SEMS are thermionic sources in which electrons are emitted from very hot filaments made of either tungsten (W) or lanthanum hexaboride (LaB_6). W sources are typically heated to ca 2500–3000 K to achieve an adequate electron brightness. LaB_6 sources require lower temperatures to achieve the same brightness, although they need a better vacuum than W sources. Once created, these primary electrons are accelerated

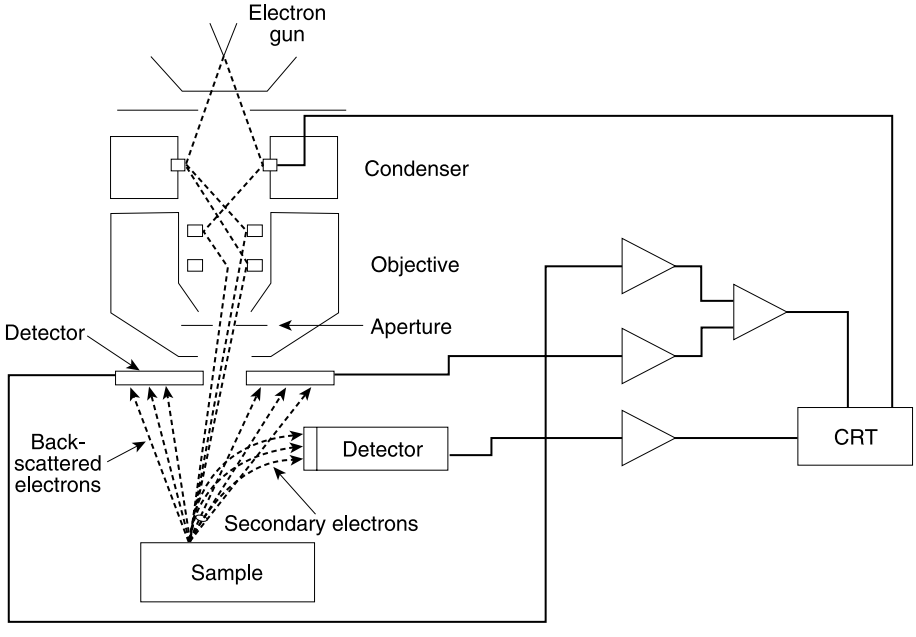

Fig. 1. Block diagram of scanning electron microscope.

to some desired energy with an energy spread (which ultimately determines lateral resolution) on the order of ca 1.5 eV.

One important SEM source that is not based on thermionic emission is the field emission (FE) source. FE-SEM systems typically give images of much higher resolution than conventional SEMs due to the much narrower energy distribution (of the order of 0.25 eV) of the primary electron beam. A field emission source is a pointed W tip from which electrons tunnel under the influence of a large electric field. This different mechanism of electron generation results in an increased brightness and a beam diameter comparable with a conventional thermionic source with much less current.

Once the primary electron beam is created, it must be demagnified with condenser lenses and then focused onto the sample with objective lenses. These electron lenses are electromagnetic in nature and use electric and magnetic fields to steer the electrons. Such lenses are subject to severe spherical and chromatic aberrations. Therefore, a point primary beam source is blurred into a primary beam disk to an extent dependent on the energy and energy spread of the primary electrons. In addition, these lenses are also subject to astigmatism. All three of these effects ultimately limit the primary beam spot size and, hence, the lateral resolution achievable with SEM.

The detectors used in SEM are of two types depending on whether secondary or backscattered electrons are being detected. As mentioned, backscattered electrons are detected with an annular detector placed above the sample such that electrons backscattered along the surface normal can be detected. Secondary electrons are detected with a detector that is positively charged to attract these electrons. This detector is placed at large angles with respect to the surface normal to most efficiently detect secondary electrons whose paths are predominantly away from the surface normal as discussed. The absolute efficiencies of both detectors are relatively low; therefore, the signals must be amplified before being sent to an image intensifier (CRT) for viewing. For SEM, the electron scan rate in the CRT is set to match the raster rate of the primary electron beam across the surface so that an image in real time is observed.

An SEM can also be equipped with additional instrumentation for electron-excited x-ray analysis (7). In many systems, this is performed in the mode known as energy dispersive spectroscopy (EDS). Wavelength dispersive x-ray analysis (WDX) is used in high-energy resolution instruments.

EDS or WDX are based on the emission of x rays with energies characteristic of the atom from which they originate in lieu of secondary electron emission. Thus, these techniques can be used to provide elemental information about the sample. In the SEM, this process is stimulated by the incident primary beam of electrons. This process is also the basis of essentially the same technique but with higher beam current and performed in a dedicated x-ray spectrometer for bulk analysis, known as electron microprobe analysis (EMA).

SEM/EDS typically occurs in a volume of sample larger than that from which backscattered electrons are observed. Thus, SEM/EDS samples the surface to a greater depth than does SEM imaging. Signals typically result from the upper several microns of the near-surface region. Therefore, this technique, similar to electron probe micro analysis (EMA), is not further considered here because it is a bulk analysis rather than a surface analysis technique.

A second important mode of electron microscopy is TEM (8). An image of a sample in TEM is obtained using the transmission of electrons by a sample in a method analogous to optical microscopy using photons. Thus, this method provides a magnified image of a transparent sample with an electron beam using objective and projector lenses as shown in Figure 2. Obviously, the requirement

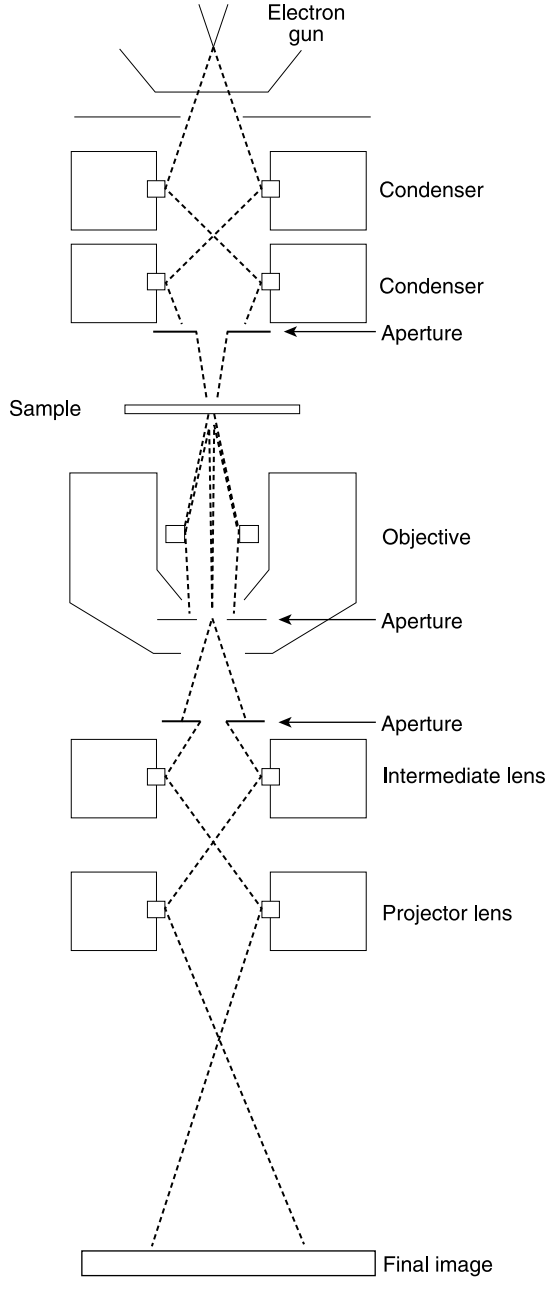

Fig. 2. Block diagram of a transmission electron microscope.

for an electron beam–transparent sample is the most important limitation of this approach. For most materials, this means that the sample thickness must be on the order of ca 20–200 nm. Given the extremely small thickness of TEM samples, the surface area-to-bulk volume is rather large; therefore, TEM contains some information of the surface as well.

Instrumentation for TEM is somewhat similar to that for SEM; however, because of the need to keep the sample surface as clean as possible throughout the analysis to avoid imaging surface contamination as opposed to the sample surface itself, ultra-high-vacuum conditions (ca 10^{-7}–10^{-8} Pa) are needed in the sample area of the microscope. Electron sources in TEM are similar to those used in SEM, although primary electron beam energies needed for effective TEM are higher, typically on the order of ca 100 keV and up to about 1 MeV for 0.1-nm point resolution (10).

Several lenses are used in a transmission electron microscope. The condenser lenses provide uniform illumination of the sample over the area of interest. The objective lens provides the primary image and, therefore, determines the lateral resolution of the image. The objective lens aperture is important in controlling the contrast of the image. The final magnification of the image is performed by one or more projector lenses. The final image is typically recorded on a fluorescent or phosphorescent screen where it can be captured by a video camera for viewing. As noted, all of these lenses are subject to serious aberrations that ultimately limit the resolution of the microscope to greater than the diffraction limit (the theoretical resolution limit for this approach.) Moreover, these lens aberrations restrict the angular range of the electron beam resulting in the need for very tall instruments. Despite these shortcomings, TEM is a very powerful surface imaging tool with atomic resolution in most modern TEM equipment, providing sample magnifications between 100 and 500,000 times. One main application in materials science is the study of the atomic structure of interfaces by "looking" edge-on to the interface along atomic rows in carefully prepared and adjusted samples (11). Chemical analysis of the interfaces, typically with nanometer resolution, is also common by using EELS. By generation of a core-level hole of an atom, the primary electron of a well-defined energy suffers an energy loss characteristic of the element, which is usually determined with an electrostatic sector analyzer attached below the image plane (12).

Scanning Probe Microscopies. A relatively new group of techniques for surface imaging is the scanning probe microscopies (13–20). The most common of these tools are STM and AFM. These techniques were developed in the 1980s and have undergone explosive growth and acceptance since the discovery of atomic resolution images by Binnig and Rohrer (13), who invented STM in 1981 at IBM Zurich. These researchers received the 1986 Nobel Prize in Physics for their work. The significance of this discovery is a readily accessible technique capable of generating real-space images of a surface with atomic-scale resolution.

STM is based on the tunneling of electrons between a very sharp, electrically conductive tip (hopefully terminating in a single atom) and a conductive sample when the tip is brought very close (<1 nm) to the sample. A schematic for this technique is shown in Figure 3. The magnitude of the tunneling current will vary in a well-defined exponential manner with tip-to-sample distance. Thus, the magnitude of the tunneling current can be used to generate an

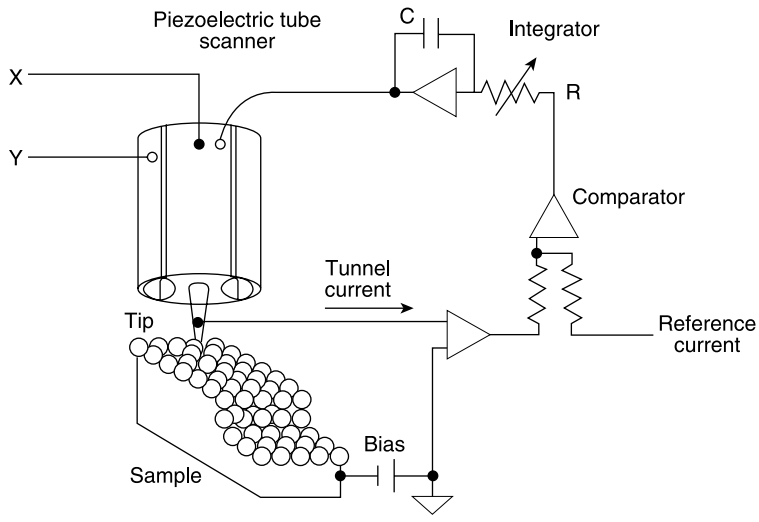

Fig. 3. Block diagram of a scanning tunneling microscope (18).

image of the surface. STM requires that both the tip and the sample be electrically conductive. Therefore, the samples that can be studied with STM are restricted to either conductors or semiconductors. The exponential dependence of tunneling current on distance between the tip and the sample gives outstanding (ie, sub-nanometer) vertical resolution. Lateral resolution is not as good and is limited by the size of the tip. Because sharp tips with a single atom at the foremost point can be prepared, atomic resolution is possible.

STM experiments can be performed in one of two common operating modes, the constant height and the constant current mode, as shown in Figure 4. In the constant height mode of operation, the tip height is maintained at a constant level above the surface and differences in tunneling current are measured as the tip is scanned across the surface. This approach is not as sensitive to surface irregularities as the constant current mode, but it is faster and it does work well for relatively smooth surfaces.

In the constant current mode of operation, the instrument uses electronic feedback to keep the tunneling current constant by moving the tip closer or further away from the surface as the tip is scanned across the sample surface. Therefore, in the simplest analysis, the height of the tip is a direct measure of the sample surface topography. This method of operation is somewhat more time-consuming than the constant height mode described above, because of the time that it takes to move the tip up and down. However, this approach is excellent for imaging irregular surfaces with high precision.

The simplest interpretation of STM images is in terms of surface topography. However, care must be exercised in this interpretation, because in reality, tunneling probability is measured. In principle, STM can map the electronic structure of a surface with atomic resolution, and therefore, it is possible to perform spectroscopic measurements with a technique called scanning tunneling spectroscopy (STS) (15). The many subtleties of STM data interpretation are

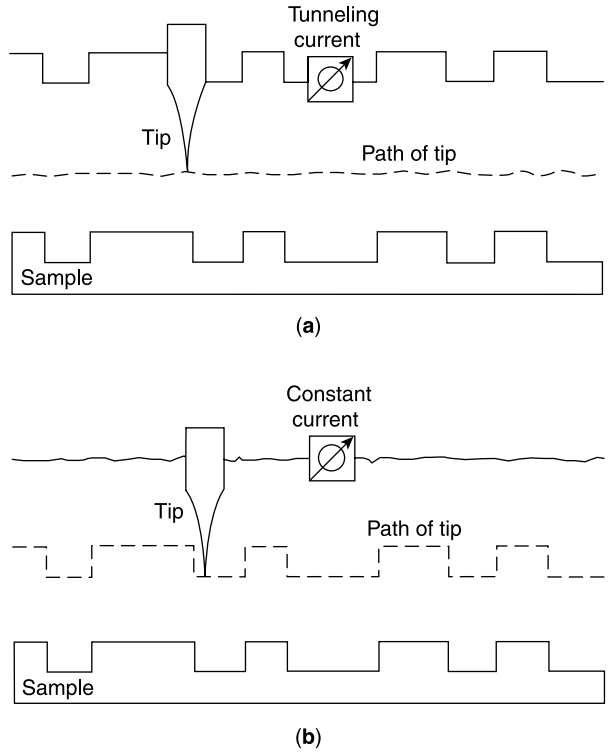

Fig. 4. Operational modes for STM: (**a**) constant height mode and (**b**) constant current mode (18).

beyond the scope of this article. The interested reader is referred to Refs. 14–17 for a more detailed discussion of these issues.

A second scanning probe microscopy that is perhaps more widely used for surface imaging today is AFM (17). This technique is related to STM, but it provides a direct topographical image of a surface without the complications arising from the electronic surface structure that cloud image interpretation in STM. In this device, a sharp tip several microns long terminating in a tip $<$10 nm in diameter is attached to a cantilever several hundred microns in length. In the original configuration of this method shown in Figure 5, the tip is dragged across the surface (or the surface dragged under the tip). van der Waals forces between the tip and the surface cause the cantilever to bend, and the extent of this cantilever deflection is measured. The real utility of this approach when compared with STM is that it can be applied to *any* surface, whether it be insulating or conductive. Thus, this technique has found successful application to conductors, semiconductors, and insulators alike. Because of the relatively low forces involved, AFM has opened a new area of surface studies of biological micro- and nanostructures, such as viruses or nucleic acids (20).

Consideration of the shape of the van der Waals force versus distance curve (Fig. 6) leads to several common operational modes of AFM. In contact-mode AFM (Fig. 5), the tip makes physical "contact" with the surface. This contact is

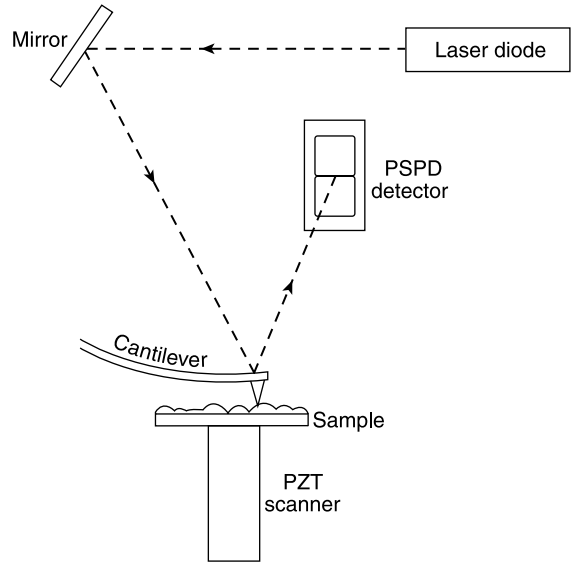

Fig. 5. Block diagram of contact atomic force microscope system in which cantilever deflection monitored optically with position-sensitive photodiode (PSPD). PZT stands for piezoelectric scanner (19).

close enough in distance to result in repulsive interatomic interactions between the tip and the sample. The cantilever bends as the tip is scanned across the surface due to these repulsive forces at different surface topologies. The bending of the cantilever is commonly sensed using an optical technique involving deflection

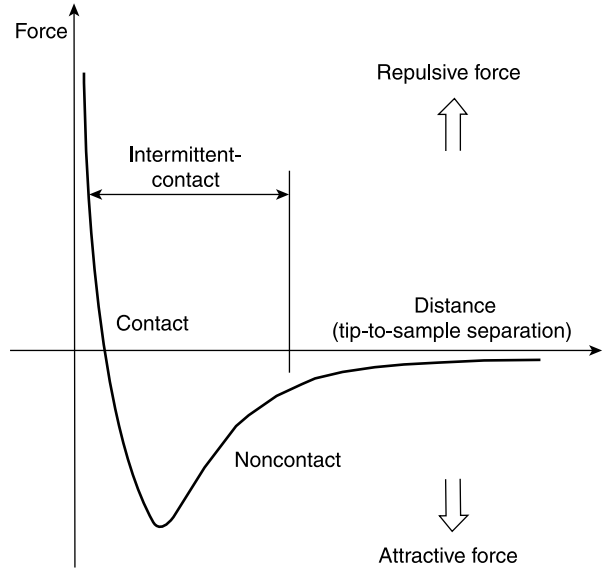

Fig. 6. van der Waals potential energy-distance curve showing regions of operation of contact, noncontact, and intermittent contact or tapping-mode AFM (16,18).

of a laser beam reflected off of the cantilever as sensed by a position-sensitive photodiode. This arrangement is sensitive to <0.1-nm vertical displacement of the cantilever position. As the tip is dragged across the surface, it experiences, in addition to repulsive forces, frictional or drag forces that can be measured as well. These are the basis of frictional force microscopy (FFM).

A second common mode of operation is tapping-mode or intermittent-contact AFM. This approach uses a vibrating cantilever that intermittently contacts or "taps" the surface, causing a change in oscillation amplitude of the cantilever in response to surface topography. These changes are monitored using an optical detection scheme similar to that described for contact-mode AFM. This mode of operation is useful, because it overcomes the potentially destructive effects of contact AFM due to the elimination of lateral forces experienced during dragging of the tip while retaining sub-nanometer vertical resolution.

New types of scanning probe microscopies are continually being developed. These tools will continue to be important for imaging of surfaces at atomic-scale resolution.

2.2. Analysis of Surface Elemental Composition. A very important class of surface analysis methods derives from the desire to understand what elements reside at the surface or in the near-surface region of a material. The most common techniques used for determination of elemental composition are the electron spectroscopies in which electrons or x rays are used to stimulate either electron or x-ray emission from the atoms in the surface (or near-surface region) of the sample. These electrons or x rays are emitted with energies characteristic of the energy levels of the atoms from which they come, and therefore, they contain elemental information about the surface. Only the most important electron spectroscopies will be discussed here, although an array of techniques based on either the excitation of surfaces with or the collection of electrons from the surface have been developed for the elucidation of specific information about surfaces and interfaces.

XPS or ESCA. XPS and Auger electron spectroscopy (AES) are related techniques (3,21–24) that are initiated with the same fundamental event, the stimulated ejection of an electron from a surface. The fundamental aspects of these techniques will be discussed separately, but because the instrumental needs required to perform such electron spectroscopies are similar, XPS and AES instrumentation will be discussed together.

XPS is based on the photoelectric effect when an incident x ray causes ejection of an electron from a surface atom. Figure 7 shows a schematic of the process for a hypothetical surface atom. In this process, an incident x-ray photon of energy hv impinges on the atom causing ejection of an electron, usually from a core electron energy level. This primary photoelectron is detected in XPS.

XPS was first successfully implemented for surface analysis by K. Siegbahn in the early 1950s. Much of the development of this approach for studying surfaces was subsequently developed by this same group (21), and Siegbahn was awarded the Nobel Prize in physics in 1981 for these efforts. He coined the term *ESCA* that also includes x-ray excited Auger electron emission. Today, the terms *ESCA* and *XPS* are generally used as synonyms.

For the primary photoelectron, which is bound to the surface atom with binding energy E_B, to be detected in XPS, the electron must have sufficient

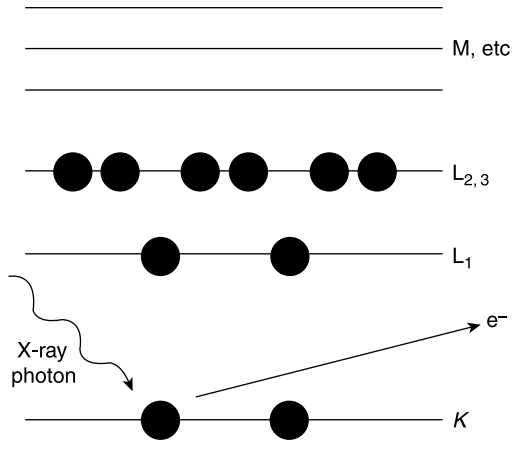

Fig. 7. Schematic of x-ray photoelectron spectroscopy process.

kinetic energy to overcome, in addition to E_B, the overall attractive potential of the spectrometer described by its work function ϕ_{SP}. Thus, the measured kinetic energy of this photoelectron E_K is given by

$$E_K = hv - E_B - \Phi_{SP} \tag{1}$$

If the energy of the incident x rays and the spectrometer work function are known, the measured kinetic energy can be used to determine the binding energy E_B from

$$E_B = hv - E_K - \Phi_{SP} \tag{2}$$

This E_B is characteristic for each energy level in the element and can be used to determine the element from which the electron originated. Differences in E_B form the basis of elemental sensitivity in XPS.

A typical x-ray photoelectron spectrum consists of a plot of the intensity of photoelectrons as a function of electron E_B or E_K. An example is shown in Figure 8 for Ag (21). In this spectrum, discrete photoelectron responses from the core ($3s$, $3p$, $3d$, $4s$, $4p$) and valence electron energy levels ($4d$) of the Ag atoms are observed, as well as lines due to x-ray excited Auger electrons (MNN). These electrons are superimposed on a significant background from the inelastic scattering of the photo- and Auger electrons emitted by atoms in deeper layers. In any inelastic scattering event, the electron energy is decreased. Because deeply located atoms contribute to the background at lower energies, the latter is increasing with decreasing kinetic energy.

The lines of primary interest in an XPS spectrum are those reflecting photoelectrons from all electron energy levels of the surface atoms. These are labeled in Figure 8 for the Ag $3s$, $3p$, and $3d$, $4s$, $4p$ core and for the $4d$ valence electrons. The sensitivity of XPS toward certain elements, and hence the surface sensitivity attainable for these elements, is dependent on the intrinsic properties of the photoelectron lines observed. The parameter governing the relative intensities

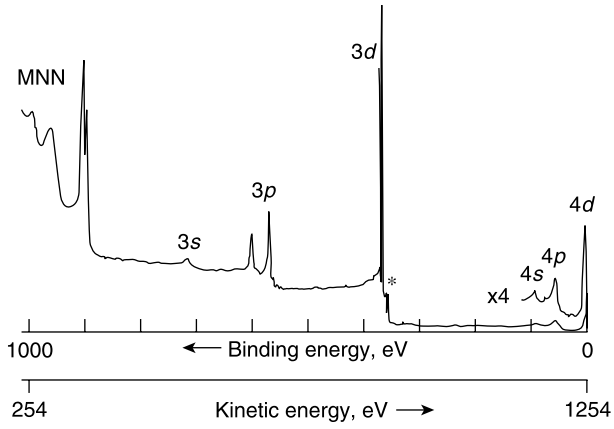

Fig. 8. XPS spectrum of Ag acquired with Mg $K_{\alpha(1,2)}$ excitation recorded with constant analyzer energy of 100 eV (* = Ag 3d peak excited with Mg $K_{\alpha(3,4)}$ satellite line) (3).

of these core-level peaks is the photoionization cross section σ. This parameter describes the relative efficiency of the photoionization process for each core electron as a function of element atomic number. Obviously, the photoionization efficiency is not the same for electrons from the same core level of all elements. This difference results in variable surface sensitivity for elements even though the same core-level electrons may be monitored.

The values commonly used for σ are those calculated by Scofield (25) or Gryzinski (26). For example, Figure 9 shows Scofield's calculated σ values

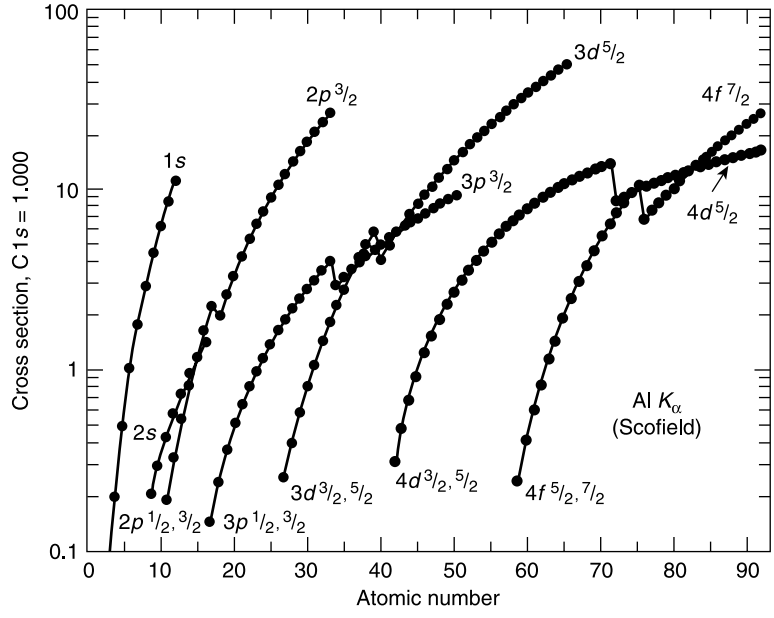

Fig. 9. Scofield's x-ray photoionization cross section relative to that for C 1s electrons as a function of atomic number (19).

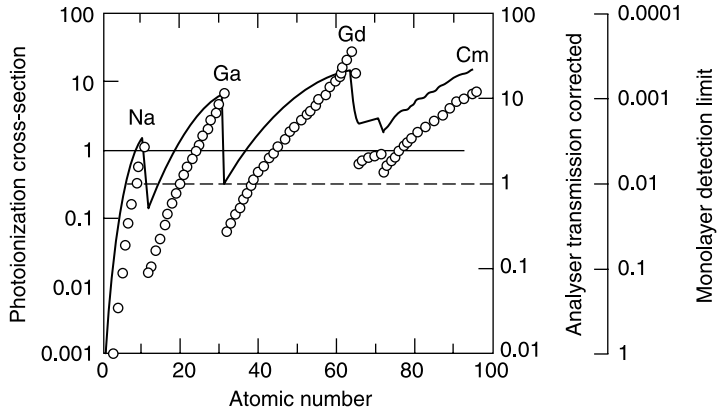

Fig. 10. Comparison of Scofield's calculated x-ray photoionization cross sections relative to that for F 1*s* electrons and experimental values (25) as a function of atomic number (1).

relative to C 1*s* electrons for Al K_α x-ray radiation. Periodic Table and core-level trends are readily apparent in these values. For a given core level, σ generally increases with atomic number (Z).

Figure 10 shows a comparison of Scofield's calculated values with experimentally measured values (27), which in addition to σ, are dependent on spectrometer transmission function. The overall agreement between the calculated and experimental values is good. The far right y-axis in Figure 10 indicates the experimentally accessible surface sensitivities in monolayers (ML) as a function of atomic number. For most elements, sensitivities between 0.1% and 1% of an ML are achievable.

Inelastic Mean Free Path (IMFP) and Attenuation Length (AL). XPS and AES are surface-sensitive techniques as opposed to bulk techniques because electrons cannot travel very far in solids without undergoing energy loss. Thus, even though the incident x rays penetrate the sample up to relatively large depths, the depth from which the electron information is obtained is limited by the "escape depth" of the photoemitted electrons. This surface sensitivity of XPS and AES is quantitatively defined by the attenuation length (AL, see below), the major contribution to which is the inelastic mean free path (IMFP) parameter, which is denoted by the symbol λ_{in}. This parameter is defined to be the mean distance an electron travels before engaging in an interaction in which it experiences an energy loss.

λ_{in} is a complex quantity that one would expect to depend on the nature of the solid sample. However, using an extensive database, Seah and Dench (28) compiled a "universal curve" of λ_{in} (actually of the attenuation length, see below) as a function of electron energy in a benchmark paper published 1979. This universal curve still gives approximately correct values for elements (but not for inorganic and organic compounds). Since 1991 it has been gradually replaced by the so-called TPP-2M relation (after the second modification published first in Ref. 29 by Tanuma et al.).

The IMFP values between 10 and 2000 eV for any material are fitted to a modified Bethe equation for inelastic electron scattering in matter:

$$\lambda_{\text{in}} = \frac{E}{E_p^2[\beta \ln(\gamma E) - (C/E) + (D/E^2)]} \tag{3}$$

where $E_p = 28.8\ (N_{\text{v}}\rho/M)^{1/2}$ is the free electron plasmon energy in electronvolts, N_{v} is the number of valence electrons per atom, M is the atomic mass, ρ is the density in grams/cubed centimeters, and E is the electron energy in electronvolts. Numerical values of the parameters β, γ, C, and D are obtained by fitting the computed IMFPs for each material to available experimental data (30). IMFPs can be estimated from TPP-2M (eq. 3) for elements, alloys, and inorganic and organic compounds with an uncertainty of typically 10% (30). Figure 11 shows the energy dependence of the IMFP for four metallic elements, calculated with eq. 3.

Note that the IMFP (eq. 3) does not consider elastic scattering. Until about 20 years ago, the influence of elastic scattering on the attenuation of the measured intensity was neglected and only inelastic scattering was considered. All measurements, however (for example, overlayer measurements), yield the AL [or better the effective attenuation length (EAL), including dependence on overlayer thickness]. Therefore, the empirical formula of Seah and Dench (28) that is still of some popularity today is not giving IMFP values (as it claims) but AL values.

In XPS, the effects of elastic scattering are particularly pronounced because the photo-ionization process is anisotropic. In general, the dependence of AES and XPS signal intensities on film thickness will not be exactly exponential, although, particularly in AES, the dependence is exponential with good approximation. In any case, inelastic and elastic scattering have to be considered

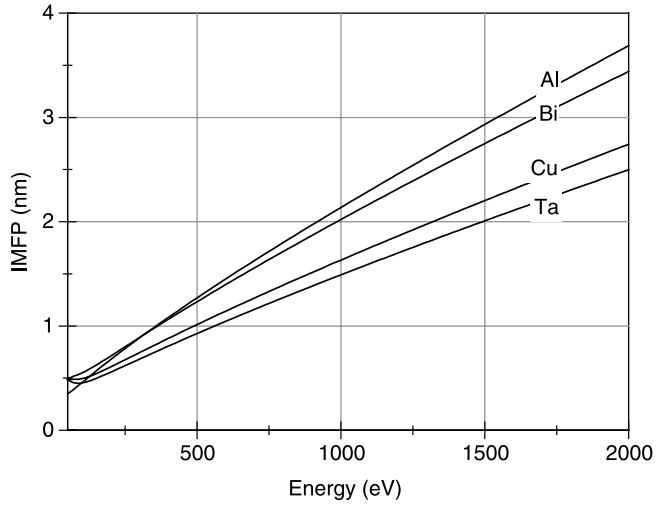

Fig. 11. Inelastic mean free path (IMFP) of Al, Bi, Cu, and Ta, as a function of the kinetic electron energy between 50 and 2000 eV calculated after eq. 3.

together and the resulting λ is the EAL. Owing to the additional elastic scattering of the electrons, their total pathlength before emission from the solid increases. As that increases the elastic scattering probability, the resulting traveled distance from the surface is less than without elastic scattering. Without elastic scattering, IMFP and EAL would be equal. When starting from IMFP values, a separate term is needed describing elastic scattering influence, to get the EAL needed for quantitative AES and XPS. According to Seah (p. 211 in Ref. 3, Vol. 1), the EAL λ can be approximately obtained from the IMFP λ_{in} by multiplication with the ratio

$$\lambda/\lambda_{in} = \left(1 - 0.028Z^{0.5}\right)[0.501 + 0.068\ln(E)] \tag{4}$$

Equation 4 shows that the ratio decreases when the atomic number Z increases and that it only weakly depends on the kinetic electron energy E (in electronvolts).

The difference between EAL (λ) and IMFP (λ_{in}) can be up to about 30% ($\lambda/\lambda_{in} = 0.7$). On average, the difference is 15–20%.

Currently, the most reliable data for EALs of elements and compounds are found in the NIST database (31).

The EAL is defined as the average emission function decay length when the emission depth distribution function (EDDF) is sufficiently close to exponential for a given application and depends on the film thickness. An average value, the practical EAL can be taken as the AL defined by a Lambert–Beer law with ($I/I_0 =$ const × exp($-z/\lambda$(AL)). According to Jablonski and Powell (32), if there is no likelihood of confusion, the term *EAL* can be further abbreviated to "AL."

Exact definitions of the relevant terms after ASTM and ISO can be found in Refs. 24 and 32.

An equation for the direct calculation of the practical EAL or AL (in nanometers) has been proposed by Cumpson and Seah (33). It is valid up to an emission angle of about 70 degrees with respect to the normal to the sample surface:

$$\lambda_{AL} = 0.316a^{3/2}\left\{\frac{E}{Z^{0.45}[\ln(E/27) + 3]} + 4\right\}[\text{nm}] \tag{5}$$

The parameter a is the average atomic distance (in nanometers) given by

$$a = 10^9\left(\frac{M_{Av}}{\rho N_A}\right)[\text{nm}] \tag{6}$$

In eqs. 5 and 6, E is the energy in electronvolts, Z the atomic number, M_{Av} the average atomic mass in kilograms, ρ the density in kilograms/cubed meter and N_A the Avogadro constant (6.02×10^{26}). Equations 5 and 6 were found to fit the average ALs computed after IMFP of TPP-2M and extension to inelastic scattering with a standard deviation of 6% at energies of 200 eV and 1 keV (33).

Frequently, the measured ALs (in nanometers) are described by a simple exponential dependence on energy (30):

$$\lambda = k\,E^m\,[\text{nm}] \tag{7}$$

where λ is the AL in nanometers, E the energy in kiloelectronvolts, and k and m are parameters. According to Tanuma et al. (30), for 500 to 2000 eV, this relation is valid with k ranging from 1.1 to 1.5 nm and an average value of $m = 0.75$ for elements and inorganic compounds and of $m = 0.79$ for organic compounds.

For the range of electron energies typically encountered in XPS (and AES) (ca 10–1500 eV), λ ranges from from ca 0.3 to 3 nm. Thus, this represents the range of depths over which the XPS experiment typically samples. About 63% of the spectral information is obtained within the range of λ.

With the λ parameter in hand, in a first-order approximation, the Beer–Lambert expression describes how the photoelectron intensity will decrease as a function of depth into the sample:

$$I = I_0 \exp\left(\frac{-z}{\lambda \cos\theta}\right) \tag{8}$$

where $I(z)$ is the intensity at a distance z above the origin of the electron, I_0 is the intensity at $z = 0$, and θ is the collection angle (or emission angle of the electrons acquired by the analyzer) with respect to the surface normal. (Often the "take off" angle with respect to the surface plane, $90-\theta$, is used, with cosinus replaced by sinus). According to eq. 8, the information depth is proportional to $\lambda\cos\theta$. If the emission angle θ increases, the depth from which photoelectrons are observed decreases, and therefore, the surface sensitivity of the analysis increases. Thus, angle-resolved XPS (ARXPS), for example, by tilting the sample in front of the analyzer, provides a crude method for depth profiling the surface region of a solid sample through control of the photoelectron emission angle (34). ARXPS is frequently applied to determine overlayer thicknesses in the range up to 5 nm, for example, ultra-thin SiO_2 oxide layer thickness on Si (35). The sampling depth proportional to the escape depth given by eq. 8 can also be varied by varying the AL using different photon energies. Synchrotron radiation offers a unique possibility for photon energy variation (see below under Instrumentation).

Another method of destruction-free depth profiling was developed S. Tougaard (36). This method is based on the quantitative description of the background on the low kinetic energy side of an elemental XPS peak as a function of the in-depth distribution of that element.

The more traditional way of depth profiling using ion sputtering is discussed further below after the section on Auger electron spectroscopy.

Chemical Shift. One other very important attribute of photoemitted electrons is the dependence of their kinetic energy on the chemical environment of the atom from which they originate. This feature of the photoemission process is called the chemical shift of E_B, which is the basis for chemical information about the sample. In fact, this feature of XPS, first observed by Siegbahn in 1958 for a copper oxide overlayer on a copper surface, led to his original nomenclature for this technique of electron spectroscopy for chemical analysis or ESCA.

Chemical shifts can be observed for atoms in both organic and inorganic materials. Generally, E_B increases as the oxidation state of the atom increases. This dependence can be rationalized on the basis of simple electrostatic considerations in terms of an increased attraction for the electron by the atom. These chemical shifts typically are between 1 and 10 eV.

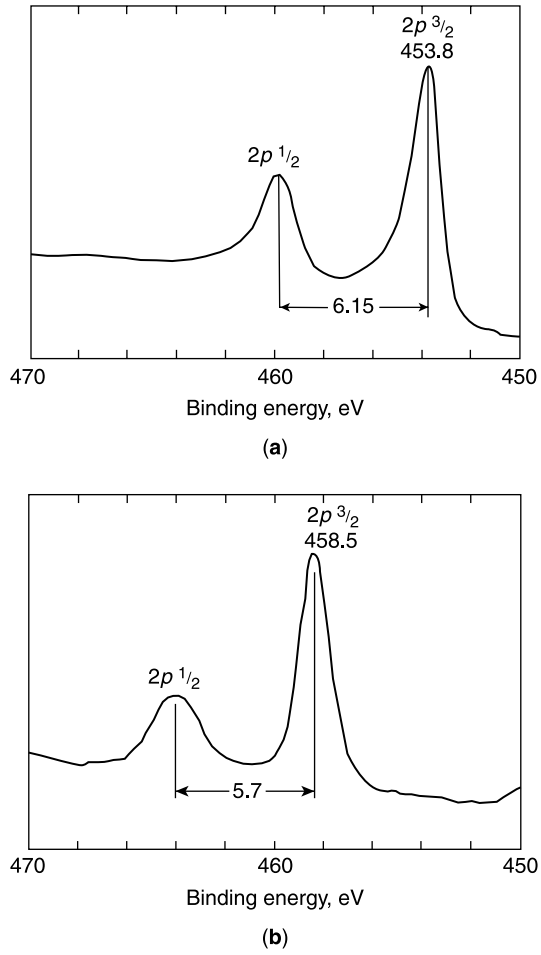

Fig. 12. XPS spectra for Ti 2*p* electrons in (**a**) Ti and (**b**) TiO_2 (21).

Figure 12 shows XPS spectra in the Ti 2*p* region for Ti and TiO_2 (22). Two peaks are observed for the Ti 2*p* electrons from spin-orbit coupling producing the $2p_{3/2}$ and $2p_{1/2}$ peaks at 453.8 and 460.0 eV, respectively. These $2p_{3/2}$ and $2p_{1/2}$ peaks shift ca 5 eV to higher binding energies of 458.5 and 464.2 eV, respectively, for electrons from Ti^{4+} atoms in the TiO_2.

Additional examples of the effect of atom oxidation state on peak position are shown in Figure 13 for two polymer systems (37). The spectrum in Figure 13**a** shows the C 1*s* region for poly(methyl methacrylate). Distinct XPS peaks are observed for the four chemically distinct C environments in this polymer. These are labeled in Figure 13**a**. The C atoms labeled as 1 exhibit a binding energy of ca 285 eV for C atoms in a hydrocarbon-like environment. The C atom labeled as 4 shows a 5-eV shift to higher binding energies from C 1 and is assigned to the C atom in the highest oxidation state, that of the carbonyl group.

A similar example is shown in Figure 13**b** for the fluorinated polymer Viton A (37). In this case, five chemically distinct C 1*s* environments exist and are seen

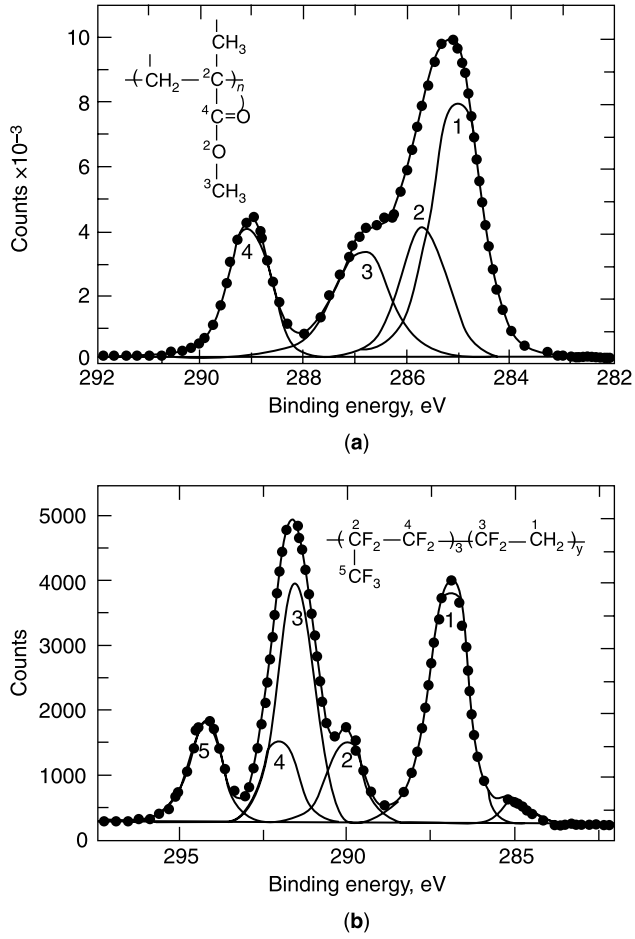

Fig. 13. (**a**) XPS spectrum for C 1*s* electrons in poly(methyl methacrylate). (**b**) XPS spectrum for C 1*s* electrons in Viton A, a fluoropolymer (37).

discretely by XPS. These are labeled in Figure 13**b**. The C 1*s* peak at 287 eV is due to C atoms bonded to hydrogen atoms. The four C atoms bonded to very electronegative F atoms exhibit C 1*s* peaks at ca 290, 291, 292, and 294 eV, higher in energy on the basis of the electronegative F atoms withdrawing electron density leaving the C atom slightly positively charged. Thus, as these examples demonstrate, XPS can be used to infer chemical information about surfaces and interfaces through the chemical shift parameter.

Quantitative XPS. XPS spectra also bear a relationship between photoelectron intensity and number of surface atoms sampled (3,24). Quantitation of these data can be achieved with a precision to within ca 10%. For a homogeneous sample analyzed in a fixed geometry, the relationship between XPS intensity and number of atoms is given by

$$I = I_0 T D \sigma L \int_0^{\infty} N \exp\left(\frac{-z}{\lambda \cos\theta}\right) dz \qquad (9)$$

where I is the XPS intensity per unit area illuminated by the x-ray source, I_0 is the incident x-ray flux, T is the transmission efficiency of the analyzer at the kinetic energy of the electron, σ is the photoionization cross section for the appropriate incident x-ray energy, L is a term that takes into account the effects of angle of incident x rays and angle of collection of photoelectrons, N is the number of atoms sampled, z is the depth from which the photoelectrons originate, and λ is the attenuation length for photoelectrons at the given kinetic energy and matrix.

It is extremely difficult to know the values for all of these parameters precisely. Therefore, absolute, "ab initio" quantitation is almost never attempted. The determination of relative atomic ratios is an inherently more tractable approach, however. This method is best illustrated by consideration of a binary material composed exclusively of atoms A and B that is perfectly homogeneous up to the surface. In this case, integration of eq. 9 yields independent equations for relating the number of atoms sampled, N_A and N_B, to the XPS intensity for each species as follows:

$$N_A = \frac{I_A}{I_0 T_A D_A \sigma_A L_A \lambda_A \cos\theta} \tag{10a}$$

$$N_B = \frac{I_B}{I_0 T_B D_B \sigma_B L_B \lambda_B \cos\theta} \tag{10b}$$

where the terms have the identities described above. For a given experiment in which both XPS lines are measured, I_0 and cos λ are identical in each equation. Furthermore, if the XPS lines of atom A and atom B are close in energy, then $T_A \approx T_B$, $D_A \approx D_B$, $L_A \approx L_B$, and $\lambda_A \approx \lambda_B$. In this case, the ratio N_A/N_B is given by

$$\left(\frac{N_A}{N_B}\right) = \frac{I_A \sigma_B}{I_B \sigma_A} \tag{11}$$

In many cases, this binary material will not be homogeneous all the way up to the surface, because it is covered with a thin overlayer of contamination. Therefore, for most real samples, the photoelectrons of interest from atoms A and B are coming from below an overlayer with thickness d, and their intensity is therefore "weakened" by the term $\exp(-d/(\lambda\cos\theta))$. In this case,

$$\left(\frac{N_A}{N_B}\right) = \frac{I_A \sigma_B \lambda_B \exp\left(\frac{-d}{\lambda_B \cos\theta}\right)}{I_B \sigma_A \lambda_A \exp\left(\frac{-d}{\lambda_A \cos\theta}\right)} \tag{12}$$

The above treatment is predicated on the assumption that the kinetic energies of the photoelectrons from atoms A and B are close in energy. In the event that this assumption does not hold, then all instrumental parameters do not cancel for these equations, and the situation is more complex. An alternative strategy in this case is to compare the spectrum of the unknown material with a spectrum acquired under identical conditions of a pure standard reference

material containing A and B that is close in suspected composition to the unknown. In this case,

$$\left(\frac{N_A}{N_B}\right)_{UNK} = \left(\frac{I_A}{I_B}\right)_{UNK} \frac{T_B D_B \sigma_B L_B \lambda_B}{T_A D_A \sigma_A L_A \lambda_A} \tag{13}$$

and

$$\left(\frac{N_A}{N_B}\right)_{STD} = \left(\frac{I_A}{I_B}\right)_{STD} \frac{T_B D_B \sigma_B L_B \lambda_B}{T_A D_A \sigma_A L_A \lambda_A} \tag{14}$$

Therefore, the relative atomic ratio of the unknown material can be determined from

$$\left(\frac{N_A}{N_B}\right)_{UNK} = \frac{(I_A/I_B)_{UNK}(N_A/N_B)_{STD}}{(I_A/I_B)_{STD}} \tag{15}$$

This approach is the most useful for routine quantitative XPS analysis. Note that all of the above equations (8)–(15) are only valid for constant, depth-independent composition. For changes of composition with depth, $N(z)$ has to be introduced for N in eq. 9.

Auger Electron Spectroscopy. AES is also based on an electron ejection process like XPS, but the electrons that are monitored in AES are secondary electrons (3,23,24). The secondary electrons called Auger electrons (named after Pierre Auger, who discovered the effect in 1923) arise from a process shown schematically in Figure 14. The process occurs after primary electron emission such

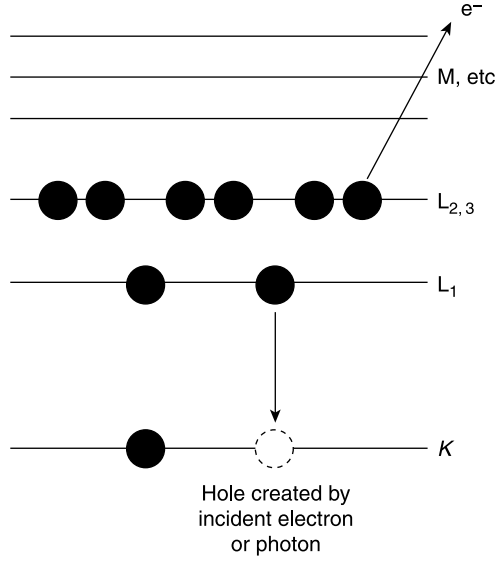

Fig. 14. Schematic of the Auger electron emission process induced by creation of a K-level electron hole.

that a core-level hole exists. Incident electrons are conventionally used in AES to stimulate primary electron emission, although incident x rays can also be used as in XPS. The presence of this core-level electron hole results in electron relaxation from an outer core level or a valence level to fill the core-level hole. When this relaxation occurs, the excess energy that is released stimulates ejection of a secondary or Auger electron from another core or valence electron energy level. The final state of the atom after Auger electron emission is thus doubly ionized; however, because these vacancies are further away from the atomic nucleus, this final doubly ionized state is more stable than the initial singly ionized state. The energy of the Auger electron is *independent* of the energy of the incident electron beam and depends only on the energies of the three electron levels involved in the process. The kinetic energy of the Auger electron is given by the difference in energy between the primarily ionized core level and the level from which the electron comes that fills the core-level vacancy minus the energy that it takes to remove the Auger electron from the singly ionized atom and the spectrometer work function ϕ_{SP}. Thus, for a KLL Auger electron

$$E_{KL(1)L(2,3)} = E_K - E_{L(1)} - E^*_{L(2,3)} - \Phi_{SP} \tag{16}$$

where $E_{KL(1)L(2,3)}$ is the kinetic energy of the Auger electron, E_K is the energy of the K core level, $E_{L(1)}$ is the energy of the electron level from which the electron comes to fill the K-level core vacancy, and $E^*_{L(2,3)}$ is the binding energy of the $L_{(2,3)}$ level *in the presence of a hole in the* $L_{(1)}$ *level*. Auger electrons typically range in energy from ca 10 to 2500 eV.

Any three subshells within an atom can be involved in the Auger process as long as the final state is significantly more stable than the initial state. The Auger transition is identified by a three-letter label in which the first letter indicates the core level in which the initial electron vacancy resides, the second letter represents the electron level from which the electron comes that fills the initial vacancy, and the third letter indicates the electron level from which the ejected Auger electron comes. KLL, LMM, and MNN Auger processes are common. Any atom has many possible Auger transitions, but the probability of each of these varies with the number of electrons in the energy levels involved. Thus, the sensitivity of AES to different atoms varies. A plot of relative sensitivity factors for different atoms normalized to the Ag 351 eV () Auger transition is shown in Figure 15 (22).

An alternative mechanism of excess energy release when electron relaxation occurs is through x-ray fluorescence. In fact, x-ray fluorescence favorably competes with Auger electron emission for atoms with large atomic numbers. Figure 16 shows a plot of the relative yields of these two processes as a function of atomic number for atoms with initial K-level holes. The cross-over point between the two processes generally occurs at an atomic number of 30. Thus, AES has much greater sensitivity to low Z elements than x-ray fluorescence. However, according to the basic process visualized in Figure 14, H and He cannot be detected.

Auger spectra are plots of the intensity of Auger electrons as a function of kinetic energy. Figure 17**a** shows a typical spectrum of a copper surface covered with contaminants (3) in the derivative mode, which is generated either by using

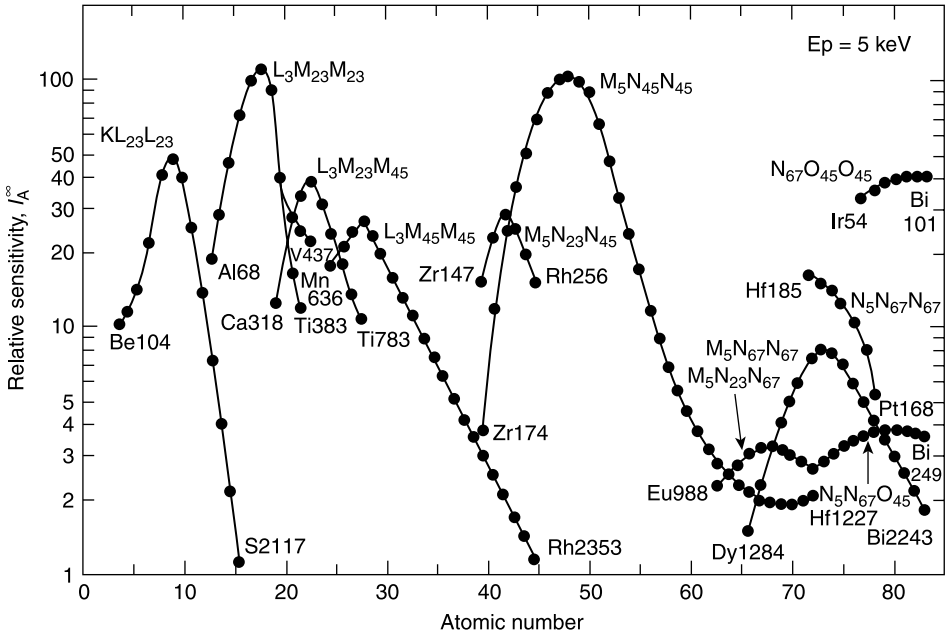

Fig. 15. Auger sensitivity factors relative to the Ag MNN Auger transition as a function of atomic number (3).

a sinusoidal modulation voltage added to the analyzer energy or by numerical differentiation of the spectrum in direct mode shown in Figure 17**b**. The Auger electrons of interest are superimposed on a very large background of elastic and inelastically scattered primary electrons used to excite the Auger process. At the lowest kinetic energies, the background increases sharply in an electron "cascade"

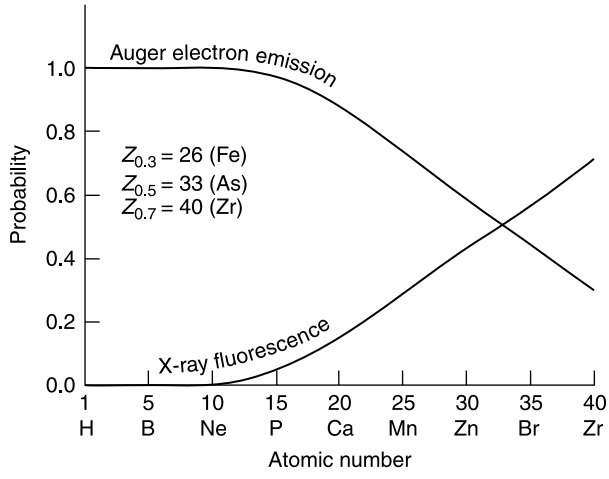

Fig. 16. Relative probabilities of Auger electron emission and x-ray fluorescence for initial *K*-level electron hole as a function of atomic number (3).

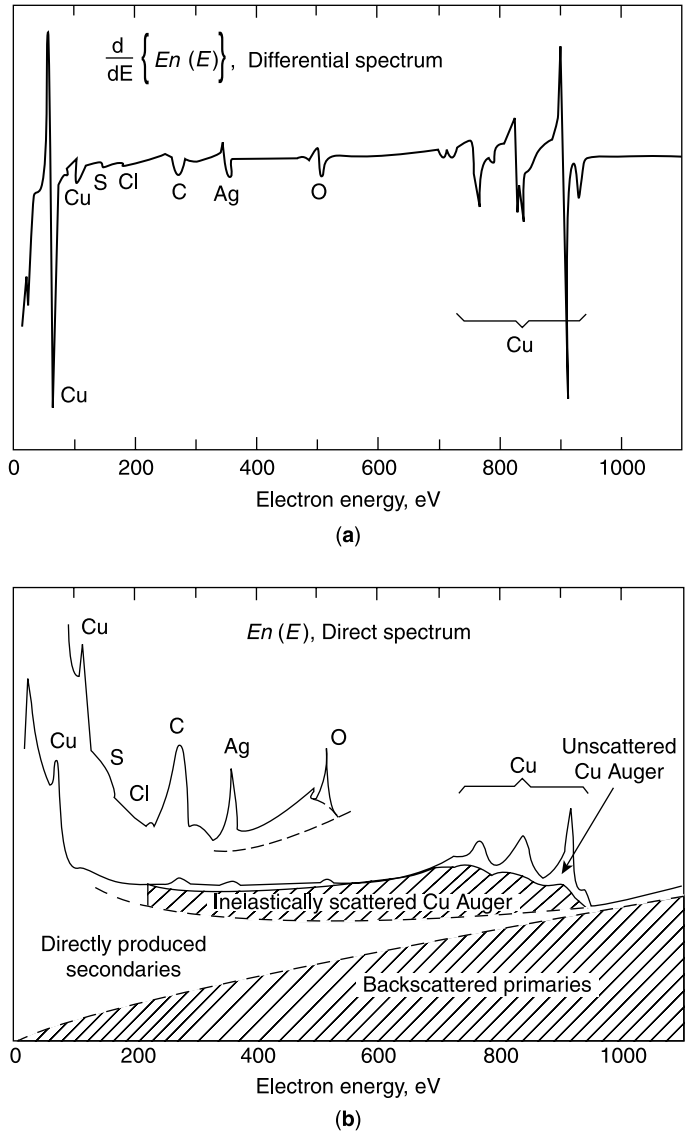

Fig. 17. (**a**) Auger electron spectrum presented in derivative mode for contaminated Cu surface. (**b**) Auger electron spectrum presented in direct intensity mode for the same sample. Contributions to background intensities indicated (3).

of inelastically scattered electrons. The intensity of the Auger electrons in relation to this electron cascade is relatively small. Therefore, Auger spectra are typically plotted as derivative spectra in which the large background contribution is "stripped" away by differentiation. The peak-to-peak height of such a derivative spectrum shown as an example in Figure 17**a** is usually taken as a measure of the respective Auger peak intensity.

Chemical Shift. Because the energy of the Auger electron depends on the three electron levels involved in the process (eq. 16), the Auger line energy

and its lineshape generally depend on the chemical environment of the emitting atom. Indeed, chemical shifts for oxides are of the order of 1 eV and above. Changes in energy and lineshape are often encountered in Auger spectra involving valence band transitions. Lineshape analysis by application of target factor analysis or least-squares fitting of standard spectral components (24) are frequently applied to distinguish chemical compounds in Auger spectra, for example, in oxidation studies of alloys (38). Mainly because of their more complex change with surface chemistry as compared with XPS spectra, Auger spectra are less frequently used for detection of chemical compounds. The influence of surface chemistry to Auger lineshapes can be a serious problem in quantification (24).

Quantitative AES. Quantitation of Auger spectra follows the same lines of reasoning as discussed above for quantitation of XPS data (3,24). Thus, the current due to Auger electrons at a particular kinetic energy I is given by

$$I = I_0 T D \sigma R_B \int_0^\infty N \exp\left(\frac{-z}{\lambda \cos\theta}\right) dz \qquad (17)$$

where I_0 is the primary electron beam current, σ_A is the total cross section for electron-induced Auger emission of the considered transition, T and D are instrumental efficiencies as defined as above, N is the atom number density, λ is the attenuation length, and R_B is the backscattering factor. This latter parameter takes on values greater than one and corrects for the creation of Auger electrons by backscattered primary electrons.

In general, eq. 17 is not used directly for quantitation of AES data due to the same limitations discussed for XPS. Particularly troubling for AES is the difficulty to determine R_B for a given matrix. Thus, the analyst is left with comparing AES data from an unknown with those of known materials in an attempt to estimate relative atom ratios. This proceeds along the same lines as for XPS and allows quantitation of AES data to a precision of typically better than ca 20%.

Sputter Depth Profiling. AES and XPS are often combined with surface ion sputtering using a high-energy ion beam to achieve profiling of the elemental composition as a function of depth into the solid (3,24,39). This approach is typically implemented using a beam of inert gas ions such as Ar^+ accelerated to 100–5000 eV to sequentially sputter away the surface layer by layer. Simultaneous with this sputtering process, scanning AES can be used to probe the depth profile of elemental composition after sputtering by a line scan at the rim of the sputtering crater that is created (crater edge depth profiling) (39).

An example of how such depth profiling information is presented and quantified is shown in Figure 18**a** for a hypothetical system composed of a substrate of element B covered by a thin film of material containing element A. This figure shows plots of AES intensity as a function of sputtering time for the ideal response and the real response expected from this system. For a given sputtering rate, the sputtering time is related to depth into the sample. If depth profiling of a chemical system with a sharp interface were ideal, and hence sputtering of the material occurred perfectly uniformly, the intensity-sputtering time profiles would mimic the physical sharpness of the interface between A and B. In reality, this does not happen due to a variety of experimental limitations.

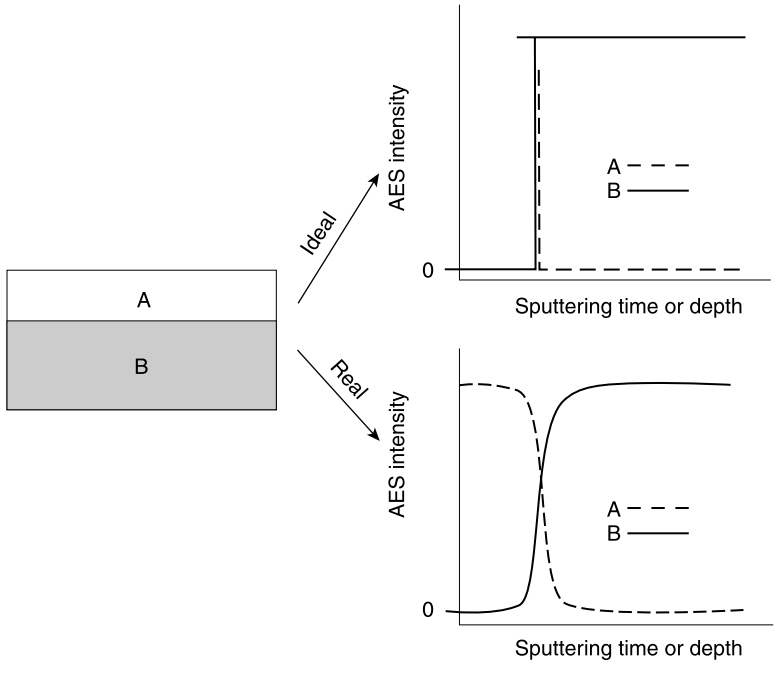

(**a**)

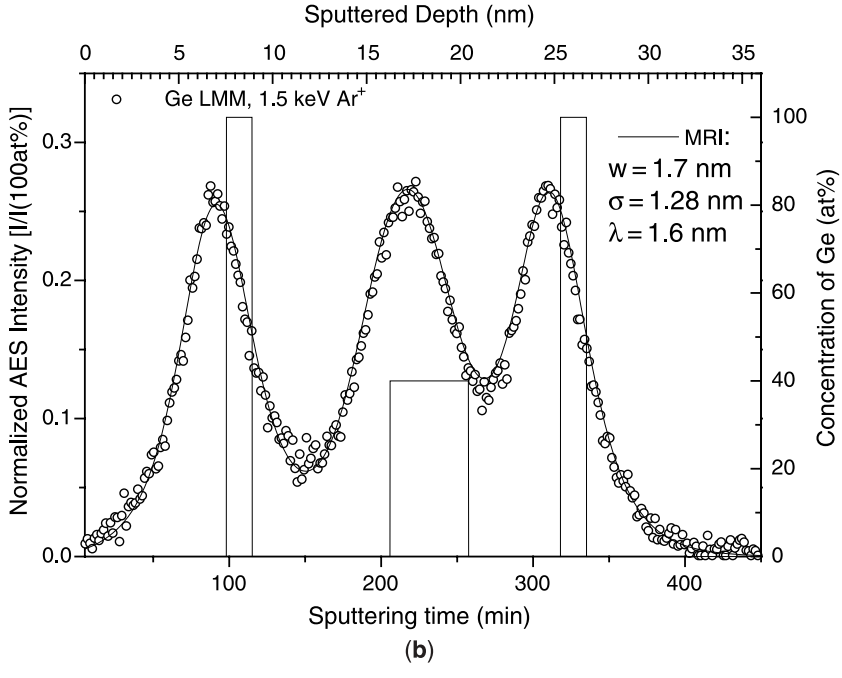

(**b**)

Fig. 18. (**a**) Ideal and real sputter-depth profiles for thin film of A and substrate B. (**b**) Sputter depth profile of a planar nanostructure of Ge in Si, quantified by the MRI model. Reprinted from Ref. 40, with permission.

First, the sputtering process is physically destructive and can lead to significant sputtering-induced atomic mixing and roughness, which blurs the interface, because parts of B can be exposed before all of A is sputtered away. In addition, A signals are still observed beyond the depth of the original interface. The situation is further complicated by the fact that many materials have different rates of sputtering, giving rise to a nonlinear depth/sputtering time relation. All of these features lead to a general broadening of the interface in the measured depth profile shown in Figure 18**a**. Mathematically, this broadening can be described by the so-called resolution function that relates the measured depth profile to the original in-depth distribution. The width of the depth resolution function is a quality figure of a depth profiling experiment.

As an example, Figure 18**b** shows a Ge nanolayer structure in a Si matrix, sputter depth profiled by 1-keV Argon ions (40). The measured Ge LMM (1145 eV) AES peak intesity (open points) is shown as a function of the sputtering time that was approximately transformed to sputtered depth (upper x-axis) by the help of TEM images. Quantitation of the measured profile was performed using the so-called Mixing-Roughness-Information Depth—or MRI—model that gives the relation between the original in-depth distribution of Ge (rectangular profile) and the measured, normalized intensity through three physically well-defined parameters. The MRI-parameters of the depth resolution function are the atomic mixing length w, the roughness parameter σ, and the information depth described by the attenuation length λ modified by the emission angle. In Figure 18**b**, these parameters have the values 1.7, 1.28, and 1.6 nm, respectively. Because of the finite values of mixing length and of information depth of AES, a shift of the measured profile toward the surface occurs.

There are many more aspects of depth profiling by a combination of ion sputtering and AES or XPS that have to be considered to obtain optimum profiling results, such as flatness of the crater in the analysis region, usually obtained by rastering of the ion beam and careful adjustment of ion and electron beams in AES and of photon beams in XPS. Using low-energy ions helps to reduce the atomic mixing parameter, and if possible, measuring low kinetic energy signals reduces the information depth parameter. Profiles on samples with rough surfaces are expected to yield widely broadened profiles, and sputtering-induced roughness is difficult to avoid. However, glancing ion beam incidence and sample rotation during sputtering have shown to effectively reduce sputtering-induced roughness and therefore increase the quality of depth profiles. The ultimate limit in depth resolution is estimated to be 0.7–1 nm (41). Preferential sputtering of a constituent is a fundamental problem. Again glancing ion incidence helps to reduce the effect, and application of the MRI model can correct for the preferential sputtering effect in a measured profile. It was shown that diffusion lengths as low as 1 nm could be determined using depth profiling quantified with the MRI model (42). For a detailed review on sputter depth profiling, the reader is referred to Ref. 39 and respective chapters in Refs. 3 and 24.

XPS and AES Instrumentation. The instrumentation required to perform XPS and AES analyses is generally sophisticated and expensive (1–3,24). The need for UHV conditions to retain surface cleanliness for a tractable period of time is *indispensable*. Beyond this requirement (and the hardware that accompanies it), the most important components of an electron spectrometer system

are the source, the electron energy analyzer, and the electron detector. These will be discussed in turn below.

XPS requires a source that can provide a single x-ray line reasonably narrow in energy. The absolute energy requirement for this x-ray line is that it must be energetic enough to generate photoelectrons from core levels of a majority of the elements with reasonable resolution. Of the many possible x-ray sources, those that best meet this requirement are the Al $K_{\alpha(1,2)}$ x-ray line at 1486.6 eV and the Mg $K_{\alpha(1,2)}$ x-ray line at 1253.6 eV. These lines have full-width-at-half-maximum (FWHM) values of 0.85 and 0.7 eV, respectively.

X rays are produced from these materials by electron bombardment using electrons whose kinetic energies are higher than the x-ray energies produced. Once produced, the x rays leave the source through an x-ray-transparent window typically made of Al. To avoid melting of the x-ray producing material, a thin film (ca 10 μm) of Al or Mg is coated onto a cooled Cu or Ag block acting as the anode. Electrons are generated at the cathode. Figure 19 shows how this is commonly done in a dual-anode arrangement in which both x-ray sources are contained within the same housing. In this case, the source can be switched in a few seconds between the Al K_α and the Mg K_α lines.

The routine dual-anode x-ray source just described generates nonmonochromatized x rays in a relatively large spot size (ca 1 cm in diameter). In fact, the Al $K_{\alpha(1,2)}$ and Mg $K_{\alpha(1,2)}$ lines are unresolved doublets resulting from the $2p_{3/2,1/2} \rightarrow 1s$ transitions in these elements. In addition to these lines, a small fraction of the x rays emitted are in the form of either a continuous background emission called Bremsstrahlung or satellite x-ray lines at other energies (eg, Al $K_{\alpha(3,4)}$). The satellite lines result in the corresponding satellite photoelectron lines in the XPS spectrum. The Bremsstrahlung x-radiation extends over a continuous band of energies above the characteristic line until the acceleration energy of the x-ray source. Bremsstrahlung contributes to the background, although its intensity is more than two orders of magnitude lower that that of the the $K_{\alpha(1,2)}$ line.

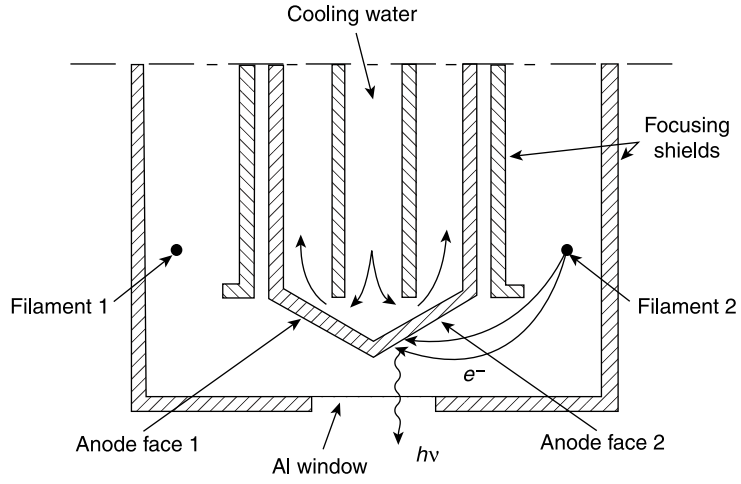

Fig. 19. Schematic of dual-anode (typically Al and Mg) x-ray source. X rays produced by electron bombardment of anode face 2 indicated (3).

To achieve higher resolution, the absence of satellite lines, and the effects of the Bremsstrahlung background in the spectrum, the use of monochromatized x rays is necessary. X-ray monochromators, commercially available for such purposes, are based on Bragg diffraction typically using a toroidal quartz crystal on a Rowland circle. Such sources, although producing narrower x-ray lines, have lower fluxes that result in lower sensitivity. Thus, the analyst must decide if the tradeoff between sensitivity and energy resolution is needed for the intended application. More recently, advances in x-ray focusing optics have resulted in the commercial availability of "small spot" XPS systems in which the spot size of the x-ray beam can be focused down to ca 5 μm in diameter. These systems, although affording considerably lessened sensitivity, provide greatly enhanced lateral surface resolution.

A special x-ray source is synchrotron radiation. In a synchrotron, electrons are confined to move in a circle by a magnetic field and are radially accelerated by the centripetal force acting perpendicular to the direction of motion. As any accelerated electron emits radiation, photons are emitted that possess a continuous spectrum with a maximum intensity at a critical wavelength (of the order of 0.1–0.4 nm or 1–10-keV energy, depending on the radius and the beam energy of the electrons). The photons are emitted in a narrow cone tangential to the electron path, pass into a monochromator, and are focused on the sample surface. The advantages of synchrotron radiation are the high photon intensity (several orders of magnitude higher than for conventional laboratory x-ray sources), the tunable excitation energy, and the polarization of the radiation in one plane. These capabilities are increasingly used, particularly in fundamental research.

The source required for AES is an electron gun similar to that described above for electron microscopy. The most common electron source is thermionic in nature with a W filament that is heated to cause electrons to overcome their work function. The electron flux in these sources is generally proportional to the square of the temperature. Thermionic electron guns are routinely used, because they are robust and reliable. An alternative choice of electron gun is the field emission source that uses a large electric field to overcome the work function barrier. Field emission sources are typically of higher brightness than the thermionic sources, because the electron emission is concentrated to the small area of the field emission tip. Focusing on both of these sources is done by electrostatic lenses. Today's thermionic sources typically produce spot sizes on the order of 0.2–0.5 μm with beam currents of 10^{-8}A at 10 keV. If field emission sources are used, spot sizes down to ca 10 nm can be achieved at a beam current of 1 nA at 10 keV that is necessary for useful Auger spectra recording. In the secondary electron detection mode at about 0.01 nA, about 3-nm beam diameters can be achieved.

The heart of the electron spectrometer system is the electron energy analyzer (2,43). The range of electron energies to be measured in XPS and AES is between 20 and 3000 eV. Analyzers are usually of electrostatic type with deflection and focusing done by electric fields to shape the electron trajectories in paths determined by the shape and size of the analyzer. The figure-of-merit for analyzers is energy resolution. Analysts refer to analyzer resolution in one of two ways: absolute energy resolution (that is the FWHM

of an electron spectroscopic peak ΔE) and relative resolution R, which is given by

$$R = \frac{\Delta E}{E_K} \tag{18}$$

where E_K is the kinetic energy at the peak position. Relative resolution is often referred to in terms of the spectrometer resolving power, which is the inverse of the relative resolution.

In most electron spectroscopic analyses, the kinetic energies of the electrons entering the analyzer are retarded to either a constant energy or by a constant factor. These approaches lead to two modes of operation: the constant analyzer energy (CAE) mode and the constant retard ratio (CRR) mode. In the CAE mode, electrons are retarded to a constant pass energy E_p that is fixed over the entire spectrum. This mode results in constant absolute resolution throughout the spectrum and is the most commonly employed mode for XPS. This retardation results in an improvement in relative resolution R by a factor equal to E_p/E_K compared with the resolution $\Delta E/E_K$ before retardation. This mode provides constant analyzer transmission throughout a spectral scan in XPS and makes the spectra easier to quantify, because ΔE is constant. The tradeoff, however, is that at low kinetic energies, the signal-to-noise ratio (S/N) of the signal degrades considerably due to the large increase in background electron intensity.

The CRR mode involves retarding the electron kinetic energies to a constant ratio of E_K/E_p where the pass energy E_p is the energy of electrons that can pass through the analyzer. Thus, the energies are retarded by a constant factor, and the relative resolution $\Delta E/E_K$ is constant throughout the spectrum. Spectra acquired in this mode are less easy to quantify, but small peaks at low kinetic energies are readily detected. The relative resolution is improved in this mode by a factor of E_p/E_K.

These modes of operation are used in conjunction with the two most popular energy analyzers, the cylindrical mirror analyzer [CMA, sometimes used in its double pass version (2)] and the concentric hemispherical analyzer (CHA). The most common form of the CMA used today (within a concentric electron gun) is shown schematically in Figure 20 (2). This device consists of two perfectly coaxial cylinders of radii r_2 and r_1. The outer cylinder is held at a potential of ($-$V), and the inner cylinder is held at ground. Electrons of kinetic energy E_K emitted from a source (ie, the sample), that lies exactly on the axis of the CMA are collected by the analyzer, usually at an angle α of 42.3° ($\pm 6^\circ$) with respect to the analyzer axis. L is the distance between sample S and focus F, equal to $6.1\, r_1$. The limiting aperture at the exit is often used to improve the resolution. The kinetic energy that is transmitted by the analyzer is given by

$$E_K = \frac{KeV}{\ln\left(\frac{r_2}{r_1}\right)} = \frac{1.31\, eV}{\ln\left(\frac{r_2}{r_1}\right)} \tag{19}$$

where the constant K is 1.31 for $\alpha = 42.3^\circ$. Obviously, a range of acceptance angles $\Delta\alpha$ (generally 6°) must be used for efficient collection. Electrons of energy

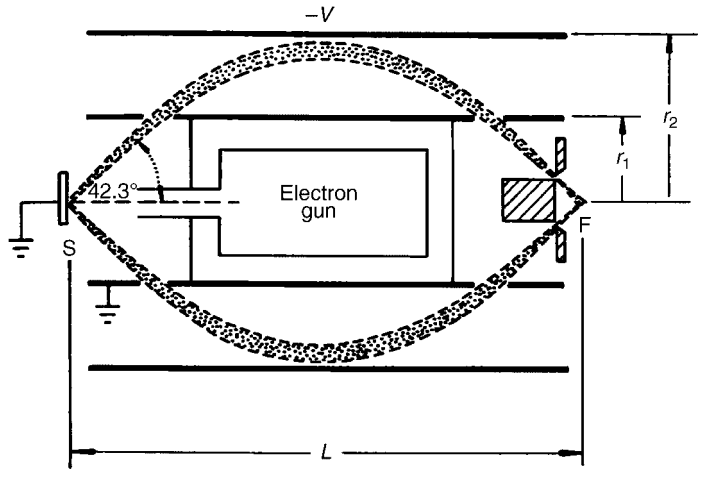

Fig. 20. Schematic diagram of a cylindrical mirror analyzer (CMA). Reprinted from Ref. 2, with permission.

above E_K suffer less deflection from the field and end up outside the exit slit, and similarly electrons of lower energy hit the inner cylinder before the exit slit. E_K is systematically varied by sweeping V for the scan of a spectrum. For a slit width of w, the energy resolution for the CMA used at this acceptance angle is given by

$$\frac{\Delta E}{E_K} = \left(\frac{0.18\,w}{r_1}\right) + 1.39\,(\Delta\alpha)^3 \tag{20}$$

In XPS in which small chemical shifts are employed to ascertain chemical information, the energy resolution of the analyzer is an important consideration. Although resolution can be increased by decreasing $\Delta\alpha$, this is done at the expense of sensitivity as dictated by the analyzer luminosity (the product of the analyzer transmission and the acceptance area). Thus, in effectively using the CMA, the analyst is faced with the need to optimize both resolution and luminosity. Although this can be fairly well achieved by a double-pass CMA, thus making it useful for XPS, today the CHA is almost exclusively used for XPS. In AES, traditional emphasis is more on the elemental detection, and therefore, in using a CMA for AES, the analyst is more concerned with transmission (and, hence, sensitivity) than with resolution. In contrast to XPS, the optimization of variables is achieved for AES in the CRR mode of operation. The large transmission of the CMA relative to the CHA makes it the more desirable analyzer for AES, although recently the CHA has also become more popular for AES because of increased count rates by parallel detection through multichannel detectors (43).

The CHA is used today for XPS in most commercial spectrometers. The most common version of the CHA is the 180° device shown in Figure 21. It consists of two concentric hemispherical surfaces of radii R_2 and R_1. These surfaces have a potential difference of ΔV applied between them so that the outer surface

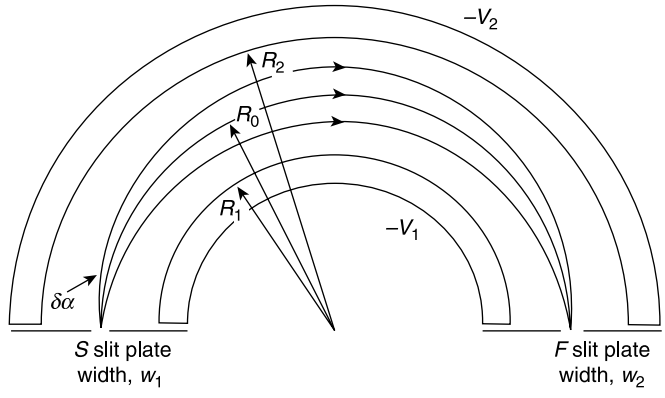

Fig. 21. Concentric hemispherical analyzer (3).

is negative and the inner surface is positive. The median equipotential surface R_0 falls between these surfaces; ideally, $R_0 = (R_1 + R_2)/2$. The kinetic energy E_K of an electron that passes through the CHA is given by

$$E_K = \frac{e\Delta V}{\left(\frac{R_2}{R_1} - \frac{R_1}{R_2}\right)} \tag{21}$$

For slits placed at R_0 from the center of curvature, the electrons passed by this analyzer follow the equipotential surface described by R_0. With an acceptance angle $\Delta\alpha$ shown in Figure 21 and a slit width w, the energy resolution of the CHA is given by

$$\frac{\Delta E}{E_K} = \left(\frac{w}{2R_0}\right) + \left(\frac{\delta\alpha^2}{4}\right) \tag{22}$$

The value of α is typically chosen to be ca $w/(2R_0)$ to optimize the compromise between sensitivity and resolution. In this case, the resolution becomes

$$\frac{\Delta E}{E_K} = \frac{0.63\,w}{R_0} \tag{23}$$

Thus, for a given R_0, an inverse relationship between resolution power $E_K/\Delta E$ and slit width w exists. Retardation with a CHA can either be in the CAE or CRR modes. This retardation is accomplished by a simple electrostatic lens system in front of the analyzer entrance slit.

The most common detector for electron spectroscopy is the channel electron multiplier. The raw currents encountered for surface-ejected electrons in a typical XPS or AES experiment are on the order of 10^{-14} to 10^{-16}A, far too low to be measured directly. Channel electron multipliers consist of a long curved surface tapering to a point coated along the entire inside with a highly resistive material

that acts as an electron amplifier. A potential difference of several thousand volts is applied across the device from front to back, which accelerates electrons. When electrons emerging from the analyzer impinge on the inside surfaces of the electron multiplier, multiple electrons are ejected. These electrons are accelerated by the potential field down the channel until the next portion of the surface is encountered at which more electrons are ejected due to the increasing kinetic energy of the electrons as they travel down the potential field. Thus, electron amplification on the order of 10^7 to 10^8 is achieved, making the currents produced by the electron multiplier easily measurable.

Multichannel detection: Today, most CHA analyzers use multichannel detection. Several multipliers (usually up to eight) are placed at the exit of the CHA in the dispersive plane. In that way, depending on the pass energy of the analyzer, an energy range of up to about 30 eV can be detected in parralel at the same time. This increases the count rate at a given resolution by about a factor equal to the number of multipliers, resulting in an increased S/N ratio (24,43).

Chemical mapping: Because of the relatively easy focusing and deflection of the electron beam, AES has been traditionally used in the scanning mode, like an SEM, to detect the spatial distribution of specific Auger lines and thus elements (or compounds, for high enough energy resolution). Spatial resolution is given by the electron beam diameter that may vary from 1 μm down to 10 nm in modern field emission gun equipment. In XPS, two different ways for chemical mapping can be used: either performing an image at a given photoelectron energy through the analyzer (eg, Kratos Axis system) or by scanning the electron beam (like in the AES), focused on an aluminium anode that generates x rays. This "point" source of x rays is focused by specially shaped monochromator crystals and directed to the sample surface, resulting in a scanning photoelectron image (PHI Quantum 2000 system). In both cases, spatial resolutions of about 5 μm can be achieved (24).

Ion Spectroscopies: ISS and SIMS. Bombardment of a surface with energetic ions results in two important effects that can be used for surface and thin-film analysis: (1) backscattered primary ions (44,45) and (2) secondary ions and neutrals (46).

(1) Some primary ions are scattered backward and lose an amount of energy that depends on the scattering angle, on the mass of the target atoms, and on the depth of the scattering event. Measurement of the backscattered ion energy distribution, most often with an electrostatic analyzer as used in AES or XPS, therefore, provides information about the atomic masses on the surface. For ions of typically a few kiloelectronvolt energy, this technique is called ISS or LEIS. For ions of higher energy, for example, of some 100-keV energy (so-called MEIS), the probing depth stretches beyond the surface to some 10 nm in the surface layer, and for typically several megaelectronvolt energy, the technique is called RBS (sometimes called HEIS) that covers thicker layers up to several micrometers (44). Therefore, the latter methods are more typically applied as thin-film profiling methods rather than as surface analysis methods.

(2) Part of the impinging ions lose their energy by inelastic collisions that result in a diffusion-like atomic mixing in the near surface layer, and some atoms in the surface obtain an energy transfer that is large enough to overcome the surface binding energy and leave the sample as ions (or as neutral atoms). Measurement of the emitted secondary ions from the target with a mass spectrometer gives information about the atoms on the surface. This is the technique of SIMS (46).

ISS. The suface specifity of ISS (44,45) is ensured by effective neutralization of ions from layers deeper than the first monolayer, particularly for the most frequently used noble gas ions He^+, Ne^+, and Ar^+ of energies between 0.3 and 2 keV. That means that ISS is the most surface-specific technique. According to the physical laws of momentum transfer, the kinetic energy E_1 of the scattered ions for 90° scattering angle is

$$E_1 = E_1^0(M_2 - M_1)/(M_2 + M_1) \tag{24}$$

where E_1^0 is the primary incidence energy of the ion with mass M_1 and M_2 is the mass of the target atom in the surface. It is obvious that all atoms with masses above H can be detected, but because of the extremely nonlinear decrease of the mass resolution for higher masses, it is difficult to distinguish adjacent atomic masses above mass number 100. (However, H can be detected by a special technique called elastic recoil detection analysis, ERDA.) The sensitivity mainly depends on the scattering cross section and on the neutralization probability and is typically of the order of a few atomic percent of a monolayer. Additional information can be obtained on the atomic positions on single crystalline surfaces by angle-resolved ISS because of shadowing effects for the scattered ions (45). Because positive ion spectroscopy can be achieved just by changing the potentials of a concentric hemispheres analyzer used in XPS, where an ion gun is also available, ISS can be performed easily with commercial XPS equipment, although specialized ISS instruments are available.

SIMS and Secondary Neutrals Mass Spectrometry (SNMS). Under energetic ion (or atom) bombardment, any surface responds by emission of secondary particles that are constituents of the sample surface: neutrals, positive and negative ions, partly in different clusters, and multiply charged. The emitted ions are separated by a mass spectrometer in terms of the ratio mass/electric charge. All elements including hydrogen can be detected. A unique feature is the capability to detect isotopes.

The elemental specifity of SIMS depends mainly on mass resolution and, to a lesser extent, on the possibility of energy-resolved detection (46).

Two principal methods of SIMS can be differentiated: static and dynamic SIMS. The main difference is the relation between sputtering rate surface erosion rate in terms thickness per sputtering time (nanometers per second or monolayers per second). Because principally SIMS is a destructive method, the sample is consumed during the analysis. In dynamic SIMS, the ion beam current density is high and many monolayers are sputtered away before spectral data are acquired. This is the technique for thin-film depth profiling. (Note that, in contrast to AES or XPS sputter depth profiling, in dynamic SIMS not the remaining

surface but the sputtered matter is detected.) Benninghoven showed in the late 1960s and early 1970s that, although SIMS is basically destructive, at a very low primary ion flux (<1 nA/cm^2), spectral data could be generated in a timescale where only a small fraction of a monolayer (typically about 1%) was consumed (47). For this nearly nondestructive surface analysis technique, he coined the term "Static SIMS." Because most particles are generated in the first monolayer, static SIMS is highly surface sensitive. The sensitivity of SIMS depends mainly on the relative probabilities of ionization and de-excitation. This results not only in a large elemental sensitivity differences, but also in strong matrix effects that may cover five orders of magnitude and therefore pose great difficulties in quantification. For example, the alkali metals with low ionization energy (K, Na, Cs) have a high elemental probability to leave the surface as a positive ion and, likewise, the halides as negative ions. De-excitation probabilities are strongly matrix dependent. To decrease the latter to obtain a higher efficiency and to reduce matrix effects by providing a similar chemical environment, primary ions in SIMS are most often oxygen ions (46). Because SIMS is a basically background-free technique, low count rates can be significant, resulting in a high dynamic range in intensity of typically 6–8 orders of magnitude, in a typical average sensitivity around 1 ppma, and in some cases to the ppba level. Thus, static SIMS is one of the most sensitive surface analysis techniques, perhaps only surpassed by the technique of total reflection x-ray fluorescence analysis (TXRF), that uses the x-ray fluorescence excitation concentrated in a thin surface layer when the x-ray incidence angle is made near 90° to obtain total reflection (48).

In SIMS, only a small fraction of the sputtered species is ionized; most of them are neutrals. The detection of these neutrals would mean an increased detection sensitivity and less scatter between output intensity and concentration for different species, ie, a widely reduced matrix effect. This is approached by post-ionization techniques such as sputtered neutral mass spectrometry (SNMS). Post-ionization means that the sputtered neutrals are ionized after having left the surface, for example, in a low-pressure argon discharge (plasma) or by a cross-electron beam. Because of the relatively small matrix effect, SNMS has the advantage of being much easier in quantification of unknown multi-element samples.

Instrumentation: The basic scheme of a SIMS instrument is shown in Fig. 22 (4). Because of the much higher sensitivity, the ion gun often has a mass separator to exclude small amounts of impurities in the primary ion beam (frequently, a Wien filter) and a slight, constant electrostatic deflection of the beam to exclude neutrals. Focusing down to the submicron beam size is

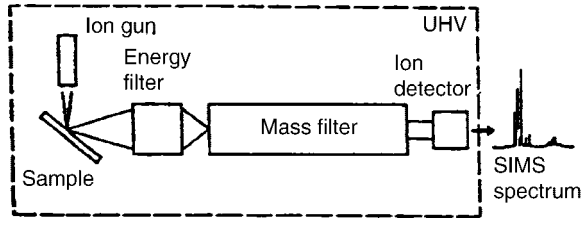

Fig. 22. Schematic representation of a SIMS instrument. Reprinted from Ref. 4, with permission.

possible, particular with liquid metal ion sources, for example, liquid gallium (46). Scanning of the primary ion beam enables compositional mapping of the surface constituents.

In front of the mass analyzer, an energy filter is generally used to preselect for monoatomic or cluster particles according to their different emission energy distributions (46). Different types of mass filter devices are used: magnetic sector analyzers, quadrupole mass analyzers, and time-of-flight (ToF) mass analyzers. For quadrupole mass analyzers, the mass resolution power is more limited and rarely is above $m/\Delta m = 1000$. Combined electrostatic and magnetic sector analyzers allow a better $m/\Delta m$ up to about 10,000. Recently developed ToF mass spectrometers have a similarly high mass resolution, with the advantage of the highest transmission (up to 50% of the emitted ions), independent of mass range and with a practically unlimited mass number that is particularly important to detect ionized fragments of high mass organic molecules as often encountered in studies of biological matter. In the technique of Time-of-Flight-SIMS (= ToF-SIMS), a pulsed high potential (typically 10-ns pulses at $E = 10$ keV) is used to accelerate the secondary ions to the same kinetic energy, $(m/2v^2) = eE$ (with e being the electrical elementary charge). After letting them fly through a field free drift tube, they arrive at the detector at a time depending inversely on their velocity that is in turn proportional to the square root of the mass. Recently, ToF-SIMS has been developed to a highly efficient technique for imaging SIMS with submicron resolution and for depth profiling with unsurpassed elemental sensitivity. For further details, the reader is referred to a recent book (49).

Electron Microprobe Analysis (EMA). Electron micro-probe analysis (EPMA) is a technique based on characteristic x-ray emission from atoms in the near-surface region of a material stimulated by a focused beam of high-energy electrons (50,51). Essentially, this method is based on electron-induced x-ray emission as opposed to x-ray-induced x-ray emission, which forms the basis of conventional XRF spectroscopy. Because the typical sampling depth is of the order of 1 μm, EMA is not considered as a surface analysis method (1–4). The relatively low lateral resolution of similar magnitude precludes its use for edge-on interface studies with nanometer resolution. Therefore, EMA is not further considered her, and the reader is referred to other articles (50,51).

2.3. Analysis of Surface Molecular Composition. Information about the molecular composition of the surface or interface may also be of interest. A variety of methods for elucidating the nature of the molecules that exist on a surface or within an interface exist. Techniques based on vibrational spectroscopy of molecules are the most common and include the electron-based method of HREELS and the optical methods of FTIR and Raman spectroscopy. These tools are tremendously powerful methods of analysis because not only does a molecule possess vibrational modes that are signatures of that molecule, but also the energies of molecular vibrations are extremely sensitive to the chemical environment in which a molecule is found. Thus, these methods directly provide information about the chemistry of the surface or interface through the vibrations of molecules contained on the surface or within the interface.

The most common and readily accessible methods are those based on FTIR spectroscopy. Several of the more common methods are discussed here.

FTIR. The most straightforward method for the acquisition of IR spectra of surface layers is standard transmission spectroscopy (52–55). This approach can only be used for samples that are partially IR transparent or that can be diluted with an IR transparent medium such as KBr and pressed into a transmissive pellet. The extent to which the IR spectral region (typically, ca 600–4000 cm^{-1}) is available for study depends on the IR absorption characteristics of the solid support material. Transmission FTIR spectroscopy is most often used to study surface species on metal oxides. These solids leave reasonably large spectral windows within which the spectral behavior of the surface species can be viewed.

Pellets of such oxides are usually prepared by mixing 5–10 wt% of the oxide with KBr and pressing a pellet that is several millimeters thick. Although the preparation of such systems is not difficult, often the pellet must be pressed for long periods of time to allow the KBr to fuse around the oxide particulates. Once prepared, IR spectra of these pellets can be acquired in standard KBr pellet holders.

The advantage of this approach for characterization of surface species is the ease of sample preparation and straightforward data interpretation. Spectra of such samples resemble normal transmission IR spectra and can be quantitated using conventional methods. In addition, this approach is reasonably sensitive with surface coverages down to ca 10% of a monolayer easily observed on oxides such as silica and alumina. One important point to note is the spectral interference that water adsorbed on an oxide surface can produce. In some cases, the spectrum from surface-confined water can swamp out the spectrum of other surface species of interest. In these cases, the transmission signal will not be strong enough to be of much use. This approach also does not work well for solids that are inherently strong IR absorbers for similar reasons. In these cases, approaches other than transmission FTIR spectroscopy must be used to acquire surface vibrational spectra.

Diffuse Reflectance Infrared Fourier Transform Spectroscopy (DRIFT). An alternative approach to the acquisition of surface IR spectra for particulate or powdered samples is DRIFT (52–55). This technique was originally developed for the IR characterization of powdered organic and inorganic samples. Its use was later extended to the study of surface species and interfacial films on particulate samples that were difficult to study by other vibrational spectroscopic methods. The technique is based on the diffuse reflectance of radiation that occurs when it is directed onto a surface with a matte finish or a sample comprising a powder. This diffuse reflectance is different than specularly reflected radiation in that it penetrates and interacts with a sample before emerging. Although the radiation is within the sample, light scattering occurs such that the diffusely reflected light emerges from the sample at all angles. Therefore, efficient collection requires collection of the diffuse reflectance over the entire 2π solid angle above the sample surface. In acquiring diffuse reflectance spectra of bulk materials, the sample is often mixed with a nonabsorbing matrix such as KBr. This matrix can have the effect of increasing the amount of IR radiation that is diffusely reflected. This practice might also be done for the characterization of surface-confined films or molecules, although such samples are more often examined undiluted by such a matrix to increase sensitivity.

The amount of diffusely reflected light cannot be measured directly; instead, it is typically measured relative to a nonabsorbing reference material such as a powdered alkali halide to allow adequate correction for scattering characteristics of the powdered sample. In acquiring DRIFT spectra, both the sample and the reference must be held in sample cells that are sufficiently deep that a further increase in sample cell depth would not change the magnitude of the signal measured. Once this sample cell depth is reached, the sample is said to be sampled at infinite depth. This depth is generally ca 3 mm for most materials. The signal that is measured is the ratio of the diffuse reflectance of the sample to that of a nonabsorbing reference material. This ratio is given the symbol R_∞. Measurement in this way allows quantitation according to Kubelka–Munk theory (56,57), which is defined in terms of the Kubelka–Munk function as

$$f(R_\infty) = \frac{(1 - R_\infty)^2}{2R_\infty} = \frac{k}{s} \tag{25}$$

where R_∞ is defined above, k is the absorption coefficient, and s is the scattering coefficient. The assumptions made in this derivation are that the specularly reflected component of the signal is small and that s is constant. The first assumption is valid for most commercially available drifts attachments. The second assumption relies on the uniformity in particle size between the sample and the reference material, which can also be achieved with care in sample preparation. Importantly, Kubelka–Munk theory predicts a linear relationship between the Kubelka–Munk function and the concentration for dilute concentrations.

Several factors affect the bandshapes observed in DRIFT of bulk materials and, hence, the magnitude of the diffuse reflectance response. Particle size is extremely important, because as particle size decreases, spectral bandwidths generally decrease. Therefore, it is desirable to uniformly grind the samples to particle sizes of <50 μm. Sample homogeneity is also important as is the need for dilute concentrations in the nonabsorbing matrix.

For surface systems, the considerations described above change very little. Most surfaces are sampled directly without dilution for maximum sensitivity. For such studies, R_∞ is usually defined as the diffuse reflectance measured from the solid sample containing the surface molecules or surface film ratioed to the diffuse reflectance measured from the same solid material in the absence of the surface molecules or surface film. Using this approach, the Kubelka–Munk function is linear with surface coverage as long as the surface coverages are kept low. At higher surface coverages, the response can become nonlinear. Using this approach for the study of surface systems such as catalysts, extremely low limits of detection can be realized with sensitivities of 1% of a monolayer or less common. Thus, drifts is a straightforward method to implement, because standard attachments to most commercial FTIR spectrometers are readily available. Its ease of implementation makes it a valuable addition to the surface analyst's repertoire for powdered samples.

Attenuated Total Reflectance-Fourier Transform Infrared Spectroscopy (ATR-FTIR). ATR-FTIR spectroscopy is based on the principle of total internal reflection (58,59). Methods based on internal reflection in the ultraviolet and visible regions of the spectrum are also common in addition to those in the IR

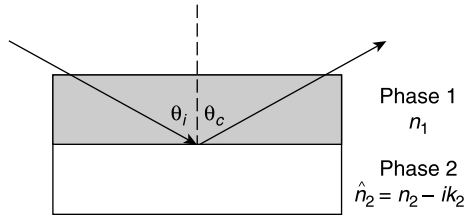

Fig. 23. Total internal reflection occurs at a boundary between the denser, transparent phase (characterized by n_1) and the rarer, absorbing phase (characterized by n_2) when θ_i is greater than the critical angle, θ_c.

region. The implementation of internal reflection in the IR region of the spectrum provides a means of obtaining IR spectra of surfaces or interfaces, thus providing molecularly specific vibrational information.

Internal reflection starts by consideration of an interface between two media, a denser transparent medium with refractive index n_1 and a rarer medium with a complex refractive index $\hat{n}_2$ ($=n_2 - ik_2$, where k_2 is the absorption coefficient of the medium) as shown in Figure 23. If k_2 of the rarer medium is zero, then the rarer medium is also transparent. For two transparent phases, total internal reflection occurs when radiation of wavelength λ_1 ($=\lambda/n_1$, where λ is the vacuum wavelength) is incident on the interface at an angle θ_i greater than the critical angle θ_c ($=\sin^{-1}[n_2/n_1]$). Although no net power is transmitted into the rarer medium, an evanescent standing wave is set up parallel to the interface, which decays in amplitude exponentially on both sides of the interface. This evanescent wave has an electric field associated with it that samples the near-interface region of the rarer medium and is the basis of spectroscopies based on internal reflection. Thus, this evanescent field is inherently interface-selective because it only samples the interface region and not the bulk.

The penetration depth of this evanescent field d_p (defined to be the depth at which the evanescent field decays to $1/e$ of its original value) is given by

$$d_p = \frac{\lambda_1}{2\pi\left[\sin^2\theta_i - (n_2/n_1)^2\right]^{1/2}} \tag{26}$$

The electric field associated with this electromagnetic wave has two notable characteristics that distinguish it from the incident beam and make it useful in the analysis of surfaces and interfaces. First, the electric field intensity (and, hence, light intensity) of the evanescent wave is enhanced relative to the incident beam. Second, the evanescent field has amplitude in all three directions in contrast to the incident traveling wave, which has amplitude in only one direction.

Attenuated total reflection, on which ATR-FTIR is based, occurs when the rarer medium is absorbing and is characterized by a complex refractive index $\hat{n}_2 = n_2 - ik_2$ (58,59). The absorbing characteristics of this medium allow coupling to the evanescent field such that this field is attenuated to an extent dependent on k_2. The critical angle in the case of attenuated total reflection loses its meaning, but internal reflection still occurs. Thus, if the internally reflected beam is

monitored, its intensity will reflect the loss associated with the internal reflection process at the interface with an absorbing medium.

The extent of the interaction between the evanescent field and the absorbing medium is formally described by the effective thickness d_e of this medium. This effective thickness is the thickness of the absorbing phase that would have to be passed through by the incident beam in a transmission experiment to give the same energy loss as in the attenuated total reflection experiment. The exact expressions for effective thickness can be very complex. However, for a single attenuated total reflection of an incident beam of radiation of electric field E_i that occurs at an interface between two bulk phases (ie, phase 2 is not a thin film), d_e is given by

$$d_e = \frac{(n_2/n_1)}{\cos\theta_i} \int_0^\infty |E|^2 dz \tag{27}$$

where $E = E_i \exp(-z/d_p)$. This expression simplifies to

$$d_e = \frac{(n_2/n_1)E_i^2 d_p}{\cos\theta_i} \tag{28}$$

when k_2 is very small (ie, $\ll 1$). It is important to note in the expression that the strength of coupling of the incident beam with medium 2 decreases (ie, smaller d_e) as θ_i increases. From this expression for effective sampling thickness, one can develop a Beer's law expression for internal reflection based on the relationship between absorbance A and reflectance R (the fraction of light reflected at an interface) as given by

$$A = -\log R \ \frac{\alpha_2 n_2 d_p I_0}{2.303 n_1 \cos\theta_i} \tag{29}$$

where $I_0 = {E^2}_i$ and $\alpha_2 = 4\pi k_2/\lambda_1$.

The real utility of d_e comes in the analysis of thin films. Consider a substrate of refractive index n_3 supporting a thin film of thickness d and refractive index n_2 in contact with an internal reflection element (the prism) of refractive index n_1 as shown in Figure 24. In this case, d_e depends on the polarization of the incident light beam and is given by

$$\begin{aligned} d_{e,\perp} &= \frac{4(n_2/n_1)d\cos\theta_i}{\left(1-(n_3/n_1)^2\right)} \\ d_{e,\parallel} &= \frac{4(n_2/n_1)d\cos\theta_i\left[\left(1+(n_3/n_2)^4\sin^2\theta_i-(n_3/n_1)^2\right)\right]}{\left(1-(n_3/n_1)^2\right)\left[\left(1+(n_3/n_1)^2\sin^2\theta_i-(n_3/n_1)^2\right)\right]} \end{aligned} \tag{30}$$

The film thickness d is what would be sampled in a simple IR transmission experiment. Thus, if d_e is the same as d, then the internal reflection experiment samples the same amount of the thin film as the transmission experiment, and

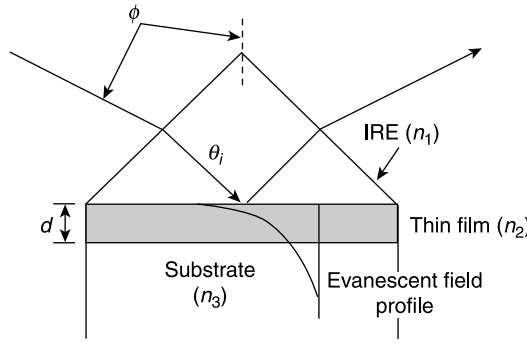

Fig. 24. Attenuated total reflectance of thin film of thickness d and refractive index n_2 on a substrate of refractive index n_3 at the surface of the internal reflection element (IRE) of refractive index n_1. Decay of evanescent field beyond thickness of thin film indicated.

no advantage accrues to the use of internal reflection. If, on the other hand, d_e is greater than d, then the effective sampling of the thin film in an internal reflection experiment is greater than in a transmission measurement, and the internal reflection experiment offers greater sensitivity. Conversely, if d_e is less than d, then a transmission measurement provides the greater sensitivity of the two measurement strategies. It should be noted that, according to the above expressions, optimization of d_e is afforded to a certain extent by alteration of θ_i and n_3.

The above discussion was based on the premise of a single internal reflection. An increase in sensitivity can be realized through the use of multiple internal reflections. In the case of multiple reflections, the absorbance A becomes

$$A = -\log R^N = -\log(1 - \alpha d_e)^N \tag{31}$$

for N reflections.

ATR-FTIR can be readily performed on most commercial FTIR spectrometers through the use of an attachment for ATR spectroscopy. These devices provide IR-transparent internal reflection elements that are typically made of Ge, KRS-5, ZnSe, or ZnS. These internal reflection elements are made of materials that are of extremely high purity to avoid losses from absorption by impurities in these devices. Coupling of a thin film or surface sample to one of these reflection elements is accomplished by pressing the sample against the element while acquiring the spectrum.

Infrared Reflection–Absorption Spectroscopy (IRRAS). For adsorbed surface species or thin films on IR reflective surfaces such as metals, an alternative method is IRRAS (60). This technique is based on the external reflection on an infrared beam of light at such surfaces, the characteristics of which are highly polarization dependent. Upon reflection of a polarized beam of light at a surface, phase shifts occur that can be significant in magnitude (61–63). Given that the electric field experienced by a molecule at a reflective surface equals the sum of the fields from the incident and reflected beams, the magnitude of this phase shift is critical in determining the resulting light intensity available with which a surface molecule can couple. Upon reflection of an s-polarized IR beam

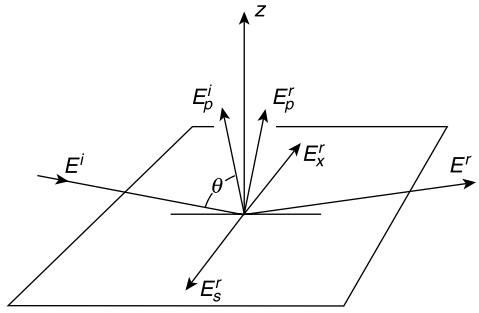

Fig. 25. Reflection geometry for IRRAS showing the *s* and *p* components of the electric fields of the incident (E^i) and reflected (E^r) beams (60).

(ie, polarized perpendicular to the plane of incidence and, hence, parallel to the surface), the phase shift is almost 180°. Thus, the resultant electric field at the surface is almost zero due to cancellation of the two electric field vectors. However, for *p*-polarized light (ie, parallel to the plane of incidence and, hence, perpendicular to the surface), the phase shift is much less than 180°. The resultant field at the surface is enhanced due to the summation of the electric fields of the incident and reflected beams. For this situation, the light intensity maximizes at near-grazing angles of incidence. A schematic of these phenomena is shown in Figure 25. These experiments can be performed using standard attachments for FTIR spectrometers that can be purchased in either fixed-angle or variable-angle geometries.

The IR spectra acquired in this way are extremely sensitive to the orientation of the surface molecules. Molecules must have a significant component of a molecular vibration perpendicular to the surface to be sensed by coupling with the highly directional electric field. Molecules whose dipole moments are perfectly parallel to the surface cannot couple to the existing electric fields, and therefore, they are IR transparent by this method. This selectivity of the approach for molecule dipole moments perpendicular as opposed to parallel to the surface is known as the surface selection rule of IRRAS.

The S/N ratio of such measurements can be further improved by making the inherently single beam FTIR system into a double-beam system using polarization modulation. In this approach, a device that alternately passes *p*-polarized and *s*-polarized IR radiation is used to alternate the polarization of light falling on the surface. The *p*-polarized light is absorbed by not only those species that are on the surface as noted above, but also by any species in the ambient phase above the surface. The *s*-polarized light is not absorbed by the surface species; thus, it is only absorbed by species in the ambient phase above the surface. Assuming that the phase above the surface is perfectly isotropic, the difference $I_p - I_s$ should provide a spectrum due exclusively to surface species.

This approach works well for species at metal surfaces. It has been used extensively in recent years to ascertain information about organic thin films on metal surfaces. Of particular interest in many of these studies, and indeed the real forte of this technique, has been the determination of molecular

orientation on surfaces from such studies. Few other techniques are so useful for unambiguously ascertaining molecular orientation.

3. Summary

An introduction to several of the more common methods of surface and interface analysis has been presented in this article. This treatment is certainly not comprehensive. An ever-expanding number of methods for the interrogation of surfaces and interfaces are available to the analyst. The ones chosen for discussion here were meant to be representative of methods that can answer the more general questions posed at the beginning of this article. The reader is encouraged to pursue further reading on other techniques for specific applications in the many excellent monographs on the subject of surface and interface analysis.

BIBLIOGRAPHY

"Surface and Interface Analysis," in *ECT* 4th ed., Supplemental Volume, pp. 541–582, by J. E. Pemberton, University of Arizona; "Surface and Interface Analysis," in *ECT* (online), posting date: December 4, 2000, by J. E. Pemberton, University of Arizona.

CITED PUBLICATIONS

1. D. J. Connor, B. A. Sexton, and R. St. C. Smart, eds., *Surface Analysis Methods in Materials Science, Springer Series in Surface Sciences*, Vol. 23, Springer-Verlag, Berlin, 1992.
2. J. C. Riviere, *Surface Analytical Techniques. Monographs on the Physics and Chemistry of Materials*, Oxford University Press, New York, 1990.
3. D. Briggs and M. P. Seah, eds., *Practical Surface Analysis*, Vol. 1: AES and XPS and Vol. 2: Ion and Neutral Spectroscopy, 2nd ed., Wiley, Chichester, 1990.
4. J. C. Vickerman, ed., *Surface Analysis: The Principal Techniques*, Wiley, Chichester, 1997.
5. C. L. Putzig, M. A. Leugers, M. L. McKelvy, G. E. Mitchell, R. A. Nyquist, R. R. Papenfuss, and L. Yurga, *Anal. Chem.* **66**, 26R (1994); C. L. Putzig, M. A. Leugers, M. L. McKelvy, G. E. Mitchell, R. A. Nyquist, R. R. Papenfuss, and L. Yurga, *Anal. Chem.* **62**, 270R (1990); D. R. Louder and B. A. Parkinson, *Anal. Chem.* **66**, 84R (1994); S. R. Snyder and H. S. White, *Anal. Chem.* **64**, 116R (1992); N. H. Turner and J. A. Schreifels, *Anal. Chem.* **68**, 309R (1996); G. E. McGuire, M. L. Swanson, N. R. Parikh, S. Simko, P. S. Weiss, R. J. Nemanich, D. R. Chopra, and A. R. Chourasia, *Anal. Chem.* **67**, 199R (1995).
6. J. F. O'Hanlon, *A User's Guide to Vacuum Technology*, 3rd ed., Wiley, New York, 2003.
7. L. E. Murr, *Electron and Ion Microscopy and Microanalysis: Principles and Applications*, Vol. 29, 2nd ed., Dekker, New York, 1991.
8. S. L. Flegler, J. W. Heckman, and K. L. Klomparens, *Scanning and Transmission Electron Microscopy: An Introduction*, Oxford University Press, New York, 1995.
9. A. J. Schwartz, M. Kumar, and B. L. Adams, eds., *Electron Backscatter Diffraction in Materials Science*, Kluwer Academic/Plenum Publishers, New York, 2000.

10. J. C. H. Spence, *High-Resolution Electron Microscopy*, Oxford University Press, New York, 2003.
11. J. Yamasaki, H. Sawada, and N. Tanaka, *J. Electron Microscopy* **54**, 123 (2005).
12. R. F. Egerton and A. Malac, *J. Electron Spectr. Rel. Phen.* **143**, 43 (2005).
13. G. Binnig and H. Rohrer, *Rev. Mod. Phys.* **59**, 615 (1987).
14. C. J. Chen, *Introduction to Scanning Tunneling Microscopy, Oxford Series in Optical and Imaging Sciences*, Vol. 4, Oxford University Press, New York, 1993.
15. D. A. Bonnell, ed., *Scanning Tunneling Microscopy and Spectroscopy: Theory, Techniques, and Applications*, Verlag Chemie, Weinheim, 1993.
16. R. Wiesendanger and H. J. Güntherodt, eds., *Scanning Tunneling Microscopy III*, 2nd ed., Springer Verlag, Berlin, 1996.
17. S. H. Cohen and M. L. Lightbody, eds., *Atomic Force Microscopy/Scanning Tunneling Microscopy*, Springer, Berlin, 1997.
18. G. A. Somorjai, *Introduction to Surface Chemistry and Catalysis*, Wiley, New York, 1994.
19. R. Howland and L. Benatar, *A Practical Guide to Scanning Probe Microscopy*, Park Scientific Instruments, 1996.
20. H. G. Hansma, *Annu. Rev. Phys. Chem.* **52**, 71 (2001).
21. K. Siegbahn, *ESCA: Atomic, Molecular, and Solid State Structure by Means of Electron Spectroscopy*, Almqvist and Wiksells, Uppsala, Sweden, 1967.
22. C. D. Wagner, W. M. Riggs, L. E. Davis, and J. F. Moulder, in G. E. Muilenberg, ed., *Handbook of X-Ray Photoelectron Spectroscopy*, Perkin-Elmer Corporation, Eden Prairie, Minn., 1979.
23. L. E. Davis, N. C. MacDonald, P. W. Palmberg, G. E. Riach, and R. E. Weber, *Handbook of Auger Electron Spectroscopy*, 2nd ed., Perkin-Elmer Corporation, Eden-Prairie, Minn., 1976.
24. D. Briggs and J. T. Grant, eds., *Surface Analysis by Auger and Photoelectron Spectroscopy*, IM Publications, Chichester, 2003.
25. J. H. Scofield, *J. Electron Spectroscopy* **8**, 129 (1976).
26. M. Gryzinski, *Phys. Rev. A* **138**, 305 (1965).
27. A. E. Hughes and C. C. Phillips, *Surf. Interface Anal.* **4**, 220 (1982).
28. M. P. Seah and W. A. Dench, *Surf. Interface Anal.* **1**, 2 (1979).
29. S. Tanuma, C. J. Powell, and D. R. Penn, *Surf. Interface Anal.* **17**, 911 (1991).
30. S. Tanuma, C. J. Powell, and D. R. Penn, *Surf. Interface Anal.* **21**, 165 (1994).
31. C. J. Powell and A. Jablonski, *NIST Electron Effective-Attenuation-Length-Database*, U.S. Department of Commerce, National Institute of Standards and Technology, Gaithersburg, Md., 2000.
32. A. Jablonski and C. J. Powell, *Surface Sci. Reports* **288**, 1 (2002).
33. P. J. Cumpson and M. P. Seah, *Surf. Interface Anal.* **25**, 430 (1997).
34. P. J. Cumpson, *J. Electron Spectroscopy* **73**, 25 (1995).
35. M. P. Seah, *Surf. Interface Anal.* **37**, 300 (2005).
36. S. Tougaard, *J. Vac. Sci. Technol. A* **14**, 1415 (1996).
37. G. Beamson and D. Briggs, *High Resolution XPS of Organic Polymers*, Wiley, New York, 1992.
38. S. Hofmann and H. J. Steffen, *Surf. Interface Anal.* **14**, 59 (1989).
39. S. Hofmann, *Rep. Prog. Phys.* **61**, 827 (1998).
40. S. Hofmann and V. Kesler, *Surf. Interface Anal.* **33**, 461 (2002).
41. S. Hofmann, *J. Surf. Anal.* **10**, 121 (2003).
42. V. Kesler and S. Hofmann, *J. Surf. Anal.* **9**, 428 (2002).
43. M. P. Seah, in J. M. Walls, ed., *Methods of Surface Analysis: Techniques and Applications*, Cambridge University Press, Cambridge, U.K., 1986.
44. A. W. Czanderna and D. M. Hercules, eds., *Ion Spectroscopies for Surface Analysis*, Kluwer Academic, 1991.

45. J. W. Rabalais, *Principles and Applications of Ion Scattering Spectrometry: Surface and Chemical and Structural Analysis*, Wiley, New York, 2003.
46. J. C. Vickerman, N. M. Reed, and A. Brown, *Secondary Ion Mass Spectrometry: Principles and Applications*, Clarendon Press, Oxford, 1990.
47. A. Benninghoven, *J. Vac. Sci. Technol. A* **3**, 451 (1985).
48. R. Klockenkamper, *Total-Reflection X-Ray Fluorescence Analysis*, Wiley, New York, 1996.
49. J. C. Vickerman and D. Briggs, eds., *ToF-SIMS: Surface Analysis by Mass Spectrometry*, IM Publications, Chichester, 2001.
50. K. F. J. Heinrich, *Electron Beam Microanalysis*, Van Nostrand, New York, 1981.
51. S. J. B. Reed, *Electron Microprobe Analysis*, 2nd ed., Cambridge University Press, 1993.
52. A. T. Bell, in J. T. Yates and T. E. Madey, eds., *Vibrational Spectroscopy of Molecules on Surfaces*, Plenum Press, New York, 1987.
53. P. R. Griffiths and J. A. de Haseth, *Fourier Transform Infrared Spectroscopy*, Wiley, New York, 1986.
54. J. R. Ferraro and L. J. Basile, eds., *Fourier Transform Infrared Spectroscopy*, Vols. 1–3, Academic Press, New York, 1978–1982.
55. A. A. Christy, Y. Ozaki, and V. G. Gregoriou, *Modern Fourier Transform Infrared Spectroscopy*, Elsevier, New York, 2001.
56. P. Kubelka and F. Munk, *Z. Tech. Phys.* **12**, 593 (1931).
57. P. Kubelka, *J. Opt. Soc. Am.* **38**, 448 (1948).
58. N. J. Harrick, *Internal Reflection Spectroscopy*, Wiley, New York, 1967.
59. F. M. Mirabella, Jr., ed., *Internal Reflection Spectroscopy*, Marcel Dekker, New York, 1992.
60. B. E. Hayden, in Ref. 52.
61. J. H. van der Maas and M. Diem, eds., *Vibrational Spectroscopy*, Elsevier, New York, 1990.
62. R. G. Greenler, *J. Chem. Phys.* **44**, 310 (1966).
63. R. G. Greenler, *J. Chem. Phys.* **50**, 1963 (1969).

SIEGFRIED HOFMANN
Max Planck Institute for Metals Research